

Turbulent energy dissipation and intermittency in ambipolar diffusion magnetohydrodynamics

G. Momferratos^{1,2*}, P. Lesaffre¹, E. Falgarone¹, G. Pineau des Forêts^{2,1}

¹ LRA/LERMA École Normale Supérieure/Observatoire de Paris,
24, rue Lhomond F 75231 Paris CEDEX 05

² IAS, Université de Paris-Sud, Centre universitaire d'Orsay Bt 120 121 91405 Orsay CEDEX

Abstract

The dissipation of kinetic and magnetic energy in the interstellar medium (ISM) can proceed through viscous, Ohmic or ambipolar diffusion (AD). It occurs at very small scales compared to the scales at which energy is presumed to be injected. This localized heating may impact the ISM evolution but also its chemistry, thus providing observable features. Here, we perform 3D spectral simulations of decaying magnetohydrodynamic turbulence including the effects of AD. We find that the AD heating power spectrum peaks at scales in the inertial range, due to a strong alignment of the magnetic and current vectors in the dissipative range. AD affects much greater scales than the AD scale predicted by dimensional analysis. We find that energy dissipation is highly concentrated on thin sheets. Its probability density function follows a lognormal law with a power-law tail which hints at intermittency, a property which we quantify by use of structure function exponents. Finally, we extract structures of high dissipation, defined as connected sets of points where the total dissipation is most intense and we measure the scaling exponents of their geometric and dynamical characteristics: the inclusion of AD favours small sizes in the dissipative range.

1 Introduction

In partly ionized astrophysical fluids, magnetic fields remain attached to the charged particles. The neutral fluid does not feel the Lorentz force and usually drifts with respect to the charges. Only the ion-neutral drag can remind the neutrals about the existence of magnetic fields. The fields are then able to slip through the bulk of the fluid: this process is called ambipolar diffusion (AD).

Mestel and Spitzer [1956] were the first to realize its importance in the context of star formation, where it would help magnetic fields to diffuse out of a contracting dense core and allow it to form a star. Mullan [1971] discovered how ambipolar diffusion could influence the dynamics of shocks which then yielded a wealth of papers on the chemical signatures of C-type shocks, starting with Draine et al. [1983] and Flower et al. [1985]. Tóth [1995] produced the first multi-dimensional simulations with AD for the stability of such shocks, and this opened the way to a collection of analytical and numerical studies in various astrophysical contexts. Brandenburg and Zweibel [1994] and Brandenburg and Zweibel [1995] envisaged that ambipolar diffusion could form very sharp structures, which would then induce the Ohmic resistivity to reconnect the magnetic field in the interstellar medium (ISM): they argued this could be a key element in solving observational problems with the galactic dynamo [Zweibel and Brandenburg, 1997]. In discs Blaes and Balbus [1994], Brandenburg et al. [1995] and Mac Low et al. [1995] showed AD was able to modulate the magneto-rotational instability. In the context of clouds and stars formation Nakamura and Li [2005], Nakamura et al. [2008], Kudoh and Basu [2008] and Kudoh and Basu [2011] computed how the magnetic support of clouds can leak out to let the gas condense and form dense cores and stars. Finally, in the context of ISM turbulence Padoan et al. [2000], Zweibel [2002], Oishi and Mac

*giorgos.momferratos@obspm.fr

Low [2006], Li et al. [2008], McKee et al. [2010], Li et al. [2012] and Li et al. [2012] focused on how magnetic fields decouple from the neutrals velocity or density and estimated the heating resulting from the ion-neutral drift.

In the diffuse interstellar medium (ISM), turbulent energy dissipation can be an important source of suprathermal energy driving hot chemistry [Falgarone and Puget, 1995]. This may be evidenced by the observed high values of the column density of species such as CH^+ and SH^+ . The formation of such species requires energy barriers of the order of at least 2000 K to be overcome, in clouds where the average temperature is known to be a few tens of K. One possible explanation is that these cold clouds contain pockets of hot gas heated by intermittent turbulent dissipation. Hot chemistry is activated there, and it is possible to construct models of turbulent dissipation that account for the high column densities of CH^+ [Godard et al., 2009].

In a turbulent magnetized fluid, dissipation can of course be due to viscosity or resistivity, but when the fluid is partially ionized and AD is at play, there can also be a significant contribution from the heat released by ion-neutral friction, as demonstrated by several authors in the context of the ISM [Scalo, 1977, Zweibel and Josafatsson, 1983, Elmegreen, 1985, Padoan et al., 2000, Li et al., 2012]. Not only does the heating help to raise the temperature which increases the rate of some chemical reactions, but the ion-neutral drift velocity provides additional energy in the reaction frame for ion-neutral reactions. In some instances, this can open new chemical routes which would otherwise be blocked by reaction barriers. The places of strong AD heating are thus expected to bear specific chemical signatures such as the ones encountered in magnetized vortices [Godard et al., 2009] or C-shocks [Lesaffre et al., 2013]. We would hence like to characterize the geometry and statistical properties of the regions of strong turbulent dissipation in the ISM.

Before us, Uritsky et al. [2010] conducted a thorough study of the statistics of strong dissipation in the context of incompressible pure magnetohydrodynamic (MHD) turbulence. In this paper we make some progress towards the physics of the ISM and we work with incompressible MHD turbulence with or without AD. We stay within the model of incompressible MHD in a first step to link our work with Uritsky et al. [2010] and to allow the use of spectral methods which are well suited for the study of small-scale dissipative structures because of their very low level of numerical dissipation. In section 2 and 3 we briefly describe the equations and the numerical method used and we present the simulations that were performed. In section 4 we present an overall picture of the dissipation fields through the time evolution of their average values, their pdfs and their spectra. We also provide a qualitative view of the dissipation field in physical space through color maps. Section 5 deals with the extreme dissipative events, it begins with a discussion of the structure functions of the velocity and magnetic fields and concludes with results from the statistical analysis of the geometrical and dynamical properties of structures of high dissipation. We discuss and conclude our results in section 6.

2 The equations

2.1 Ambipolar drift

In a partly ionized fluid, the time-dependent evolution of both the neutral and the ionized fluids should in principle be followed. However, in circumstances that we will make explicit below (see subsection 2.4), we can adopt the strong coupling approximation. In this approximation, we neglect the inertia, pressure and viscosity of the ions in the ion momentum evolution and we are left with the balance between the ion-neutral drag and the Lorentz force

$$\gamma \rho_i \rho_n (\mathbf{U}_i - \mathbf{U}_n) = \mathbf{J} \times \mathbf{B} \quad (1)$$

where the current density

$$\mathbf{J} = \frac{1}{4\pi} (\nabla \times \mathbf{B}),$$

ρ_i and ρ_n are the ion and neutral mass density ($\rho_i \ll \rho_n$), \mathbf{U}_i and \mathbf{U}_n are the ions and neutrals respective velocities, and where γ is the coefficient of ion-neutral drag

$$\gamma = \frac{\langle \sigma v \rangle_{in}}{m_i + \mu}$$

with m_i and μ the ions and neutrals mass per particle and $\langle\sigma v\rangle_{in}$ the ion-neutrals collision rate. Assuming that $n_{\text{He}} = 0.2n_{\text{H}_2}$, we find $\mu = 2.33m_p$ for molecular gas, where m_p is the mass of the proton. In diffuse clouds, the average mass per ion is $m_i = 12m_p$ as the dominant ion is C^+ . Following Draine et al. [1983], we take $\langle\sigma v\rangle_{in} = 1.9 \times 10^{-9} \text{cm}^3 \text{s}^{-1}$ and we arrive at $\gamma = 6.7 \times 10^{13} \text{cm}^3 \text{s}^{-1} \text{g}^{-1}$.

Within these approximations, the above balance (1) expresses the ion-neutral drift velocity as a function of the magnetic field. When this is plugged into the induction equation

$$\partial_t \mathbf{B} = \nabla \times (\mathbf{U}_i \times \mathbf{B}) + \eta \nabla^2 \mathbf{B}$$

one recovers the ambipolar diffusion term:

$$\nabla \times \left[\frac{1}{\gamma \rho_i \rho_n} (\mathbf{J} \times \mathbf{B}) \times \mathbf{B} \right]$$

[cf. Balbus and Terquem, 2001], which can be developed into

$$\nabla \times \left[-\frac{B^2}{\gamma \rho_i \rho_n} \mathbf{J} + \frac{\mathbf{J} \cdot \mathbf{B}}{\gamma \rho_i \rho_n} \mathbf{B} \right]$$

from which properly speaking only the first term takes the form of a diffusion, with diffusion coefficient $\lambda_{\text{AD}} = \frac{B^2}{\gamma \rho_i \rho_n}$ [Brandenburg and Zweibel, 1994], but the qualificative is usually retained for the whole term. In particular, Brandenburg and Zweibel [1994] recognized that the second term steepens the magnetic field profile near magnetic nulls. It should finally be noted that AD itself is not per se able to reconnect the field lines: this requires Ohmic diffusion.

2.2 Incompressible MHD

We now take u_0 a typical velocity and l_0 a typical length scale as unit velocity and unit length to normalize our equations. We also define $t_0 = l_0/u_0$ as the unit of time. We write the non-dimensional velocity $\mathbf{u} = \mathbf{U}_{\text{cdm}}/u_0$ where \mathbf{U}_{cdm} is the center of mass velocity

$$\mathbf{U}_{\text{cdm}} = \frac{\rho_i \mathbf{U}_i + \rho_n \mathbf{U}_n}{\rho}$$

with $\rho \sim \rho_n$ the total density of the gas, $\rho = \rho_i + \rho_n$. We write the non-dimensional Alfvén velocity $\mathbf{b} = \mathbf{B}/\sqrt{4\pi\rho}/u_0$. The non-dimensional current is simply $\mathbf{j} = \nabla \times \mathbf{b}$ where ∇ is now understood as derivatives in coordinates in units of l_0 : $\nabla \rightarrow l_0 \nabla$.

In the diffuse ISM, the sonic Mach number $\mathcal{M}_s = u_0/c_s$ (where c_s is the speed of sound) as well as the Alfvén Mach number $\mathcal{M}_a = 1/|\mathbf{b}|$ take values in the range $10^{-1} - 10$ [Elmegreen and Scalo, 2004]. This wide range of values suggests that although most of ISM turbulence is highly compressible, incompressible turbulence is not irrelevant since in a weakly compressible flow the density fluctuations $\Delta\rho/\rho \sim \mathcal{M}_s^2$ are of the order of the square of the sonic Mach number. Hence a turbulent flow with $\mathcal{M}_s < 0.3$ can be adequately described by the incompressible equations. For example, the studies of Brandenburg and Zweibel [1995], Zweibel [2002] or Godard et al. [2009] on turbulent dissipation with AD were all based on the incompressible equations of motion.

We use the equations in Balbus and Terquem [2001] and the above notations to derive the equations of incompressible, viscous, resistive, AD MHD :

$$\begin{aligned} \partial_t \mathbf{u} + (\mathbf{u} \cdot \nabla) \mathbf{u} &= -\nabla p + \mathbf{j} \times \mathbf{b} + Re^{-1} \nabla^2 \mathbf{u} \\ \partial_t \mathbf{b} &= \nabla \times (\mathbf{u} \times \mathbf{b}) + Re_a^{-1} \nabla \times ((\mathbf{j} \times \mathbf{b}) \times \mathbf{b}) + Re_m^{-1} \nabla^2 \mathbf{b} \end{aligned} \quad (2)$$

where \mathbf{u} and \mathbf{b} satisfy $\nabla \cdot \mathbf{u} = 0$ and $\nabla \cdot \mathbf{b} = 0$ and $p = P/(u_0^2 \rho)$ is the non-dimensional pressure, with P the actual thermal pressure. Equations (2) are parameterized by three non-dimensional numbers Re , Re_a and Re_m , for which we now give estimates.

2.3 Reynolds numbers

Firstly, the kinetic Reynolds number $Re = u_0 l_0 / \nu$, where ν is the molecular viscosity of the fluid, expresses the relative importance of inertial terms in comparison to the viscous term. In the neutral ISM, assuming that the most significant contribution to viscosity is given by H_2 collisions, we have $\nu \sim \frac{1}{3} \lambda_{H_2} c_s$ where λ_{H_2} is the mean free path of the H_2 molecule and $c_s = (\Gamma k_B T / \mu)^{1/2}$ is the isentropic sound speed, with $\Gamma \simeq 5/3$ the ratio of specific heats, and k_B the Boltzmann constant. The mean free path is given by $\lambda_{H_2} \sim (n_{H_2} \sigma_{H_2})^{-1}$ where n_{H_2} is the number density of H_2 and $\sigma_{H_2} = 3 \times 10^{-15} \text{ cm}^2$ is an estimate of the cross section of H_2 collisions [Monchick and Schaefer, 1980]. For molecular gas $n_{H_2} = 0.5 n_H$ where n_H is the hydrogen nuclei density. Under these assumptions, the kinetic Reynolds number is of the order

$$Re \sim 1.8 \times 10^7 \left(\frac{n_H}{100 \text{ cm}^{-3}} \right) \left(\frac{u_0}{1 \text{ km s}^{-1}} \right) \left(\frac{l_0}{10 \text{ pc}} \right) \left(\frac{T}{100 \text{ K}} \right)^{-\frac{1}{2}}.$$

Elmegreen and Scalo [2004] quote typical values of the kinetic Reynolds number in the cold ISM ranging from 10^5 to 10^7 .

Secondly, $Re_m = u_0 l_0 / \eta$ is the magnetic Reynolds number, where η is the resistivity. The magnetic Reynolds number expresses the relative importance of advection in comparison to Ohmic diffusion in the dynamics of the magnetic field. In a system with a large value of the magnetic Reynolds number, the dynamics of the magnetic field is dominated by advection and stretching. The value of the resistivity is given by

$$\eta = 234 \left(\frac{n}{n_e} \right) T^{1/2} \text{ cm}^2 \text{ s}^{-1}$$

[Balbus and Terquem, 2001], where n is the total number density and n_e is the electron density. The order of magnitude of the magnetic Reynolds number is

$$Re_m = 2.2 \times 10^{17} \left(\frac{l_0}{10 \text{ pc}} \right) \left(\frac{u_0}{1 \text{ km s}^{-1}} \right) \times \left(\frac{n_e}{10^{-4} n_H} \right) \left(\frac{T}{100 \text{ K}} \right)^{-1/2}$$

where we assumed $n = 0.6 n_H$ for molecular gas.

Lastly, the AD Reynolds number Re_a helps to measure the ratio of the ambipolar to advective electromotive forces in the induction equation:

$$Re_a = \frac{t_0}{t_a}, \quad t_a = \frac{1}{\gamma \rho_i} \quad (3)$$

where t_a can be recognized in equation (1) as the ion-neutral friction time scale. The quantities Re_a and l_a should not be confused with their more usual definitions R_{AD} and ℓ_{AD} as introduced by Zweibel and Brandenburg [1997], for example. For instance, the usual values depend on the r.m.s. velocity and magnetic field, whereas our definition encompasses only the ion-drift time: see the subsection 2.4 for more details. We can also write it as a ratio of length scales

$$Re_a = \frac{l_0}{l_a}$$

where we define

$$l_a = t_a u_0 \quad (4)$$

which gives a typical length scale for ion-neutral decoupling. The AD Reynolds number is an increasing function of the ionization fraction $x = \rho_i / \rho$. Using C^+ as the dominant ion of the ISM, we find

$$Re_a = 4.9 \times 10^3 \left(\frac{l_0}{10 \text{ pc}} \right) \left(\frac{n_{C^+}}{10^{-4} n_H} \right) \left(\frac{n_H}{100 \text{ cm}^{-3}} \right) \left(\frac{u_0}{1 \text{ km s}^{-1}} \right)^{-1}.$$

In the ISM, we have $Re_a \ll Re \ll Re_m$ which suggests the ordering $l_a \gg l_\nu \gg l_\eta$ for the ambipolar, viscous and resistive dissipation scales. However, our finite computing power does not allow much dynamics of scales and here we can only afford $l_a > l_D$ where $l_D = l_\nu \sim l_\eta$ is a single dissipative scale. In this study the magnetic Prandtl number $Pr_m = \nu / \eta$ is therefore taken equal to unity, so that the

hydrodynamic and magnetic Reynolds numbers are equal. This choice results in a single dissipative range of scales for both the velocity and the magnetic fields, a fact which simplifies the analysis considerably.

Although this numerical study is confined to Reynolds numbers that are several orders of magnitude lower than those found in the interstellar medium, it is relevant to ISM physics in the sense that it allows a detailed quantitative study of the dissipation field as well as the relative importance of the different types of turbulent dissipation, which can all be important as a heating source for ISM chemistry.

2.4 Lengths scales associated with AD

We outline here various scales introduced by AD physics. The case of C-shocks allows to clearly separate them. We have already introduced the length scale $l_a = u_0 t_a$ which corresponds to the re-coupling length scale between ions and neutrals. It is the scale of variation of the neutral's velocity in a C-shock with entrance velocity u_0 , which therefore has a length on the order of l_a [Flower and Pineau des Forets, 1995].

Under the strong coupling approximation, the scale of variation of the *ions* velocity in the same C-shock is $l_{ai} = u_0 t_a / \mathcal{M}_a^2$ where \mathcal{M}_a is the transverse Alfvénic Mach number of the shock. For shocks with a large Alfvénic Mach number, this length-scale is significantly smaller than l_a and the structure of the shock consists of a front in the ions velocity followed by a smoother transition for the neutral velocity [see Fig. 1 of Li et al., 2006, for example].

In the case of typical ISM turbulence, though, \mathcal{M}_a is of order one, and both length scales do not differ significantly. In fact, Zweibel and Brandenburg [1997] constructed the AD diffusion Reynolds number of eddies of length scale ℓ and velocity U based on the AD diffusion coefficient: $R_{AD}(\ell) = \ell U / \lambda_{AD} = \ell / \ell_{AD}$ where $\ell_{AD} = U t_a / \mathcal{M}_a^2$ with $\mathcal{M}_a = U / c_a$.¹ Zweibel and Brandenburg [1997] then argue that only eddies of length scales below ℓ_{AD} should be affected by AD. We prefer to get a similar estimate by comparing the Fourier amplitudes of the AD e.m.f. ($Re_a^{-1}(\mathbf{j} \times \mathbf{b}) \times \mathbf{b} \rightarrow Re_a^{-1} k b^3$) and the inertial e.m.f. ($\mathbf{u} \times \mathbf{b} \rightarrow ub$) in the the induction equation (2). Wave numbers above the critical wave number

$$k_a = Re_a \sqrt{\langle u^2 \rangle} / \langle b^2 \rangle \quad (5)$$

should be AD dominated. We hence define $\ell_a = 2\pi / k_a$ accordingly, as the length scale below which AD should be effective. Note that ℓ_{AD} and $l_0 \ell_a$ differ only by a factor of 2π .

Similarly, we can estimate the length scale below which the strong coupling approximation breaks down by comparing the magnitude of the neglected inertial term $D_t \rho_i \mathbf{U}_i$ to the coupling term $\rho_n (\mathbf{U}_n - \mathbf{U}_i) / t_a$. Assuming that \mathbf{U}_n , \mathbf{U}_i and $\mathbf{U}_n - \mathbf{U}_i$ all share the typical magnitude u_0 , we then get a critical wavenumber $k_{\text{two-fluids}} \simeq \rho_n / \rho_i / l_a$ above which the strong coupling approximation fails and the two-fluids approximation is needed. Provided ρ_i / ρ_n is small (it is typically lower than 10^{-3} if the main charges are C^+ ions), the strong coupling approximation breaks down at scales much smaller than the typical AD diffusion scale. Other authors [Oishi and Mac Low, 2006, Padoan et al., 2000] have claimed that the strong coupling approximation breaks down as soon as $\ell < \ell_{AD}$ or $R_{AD} < 1$, where the ions inertia does not appear explicitly. But Fig. 1 of Li et al. [2006] shows a C-shock computed with the two-fluid approximation (solid) compared to an analytical solution (dashed) using the strong coupling approximation, and the agreement is perfect. We hence believe that the strong coupling approximation is a very good one in the low ionized ISM where $\rho_i / \rho_n \ll 1$, even in cases where $R_{AD} > 1$. In particular, $k_{\text{two-fluids}}$ is at least a few ten times above the largest wave number in all our AD simulations, which amply justifies our use of the strong coupling approximation.

Finally, the observed emission of the ISM depends on the chemical and thermal state of the gas, which are strongly linked to the heating. The scale at which the heating takes place may not necessarily be directly connected to the scale ℓ_a where AD undergoes a change of dynamical regime. In fact we will see that it is not the case in the present paper, and we will be forced to introduce yet an other length scale ℓ_a^* for the typical thickness of sheets of strong AD heating.

¹For example, with $\ell = l_a$, we find that the AD Reynolds number of a C-shock is either $R_{AD} = 1$ or $R_{AD} = \mathcal{M}_a^2$ depending on whether we compute it with the post-shock or the pre-shock magnetic field strength.

3 The simulations

3.1 Method

Many compressible methods have been devised to treat AD in the strong coupling or in the two-fluids approximations: see Masson et al. [2012] and references therein. Here, we solve the strong-coupling incompressible equations (2) in 3D using a spectral method for various values of the parameters and various initial conditions. Our spectral code ANK² is fully de-aliased by use of the phase-shift method of Patterson and Orszag [1971] and uses polyhedral truncation [Canuto et al., 1988]. Polyhedral truncation considers only these wave-vectors for which the sum of any two of their components does not exceed $2N/3$. Similarly with the widely used two-thirds rule, but contrary to an isotropic spherical truncation, this truncation scheme does not possess a sharp limit in wavenumber space. Polyhedral truncation allows us to keep 55 percent of the modes active, in comparison to 33 percent for the standard two-thirds rule, resulting in a more accurate description of the small scales. The Fourier transforms are computed with FFTW with single precision accuracy, and a standard fourth-order Runge-Kutta method is used for time integration. We checked that our code gives the correct solution for Alfvén waves damped by AD. As a resolution check for all simulations, we also looked for bumps in the kinetic and magnetic energy spectra near the truncation limit. In the case of the kinetic energy spectra we found bumps no larger than 15 %, whereas no bumps were present in the magnetic energy spectra. Note that we do not include a driving force in equations (2): our simulations are freely decaying. The MHD simulations with 512^3 resolution take about 5000 CPU hours until the peak of dissipation but the equivalent AD-MHD simulations require ten times more CPU time due to the more stringent time-step requirement.

In the spectral simulations performed, the velocity and magnetic fields are defined on a regular Cartesian grid of points, while boundary conditions are periodic in all directions. Note the total length of the computational domain is 2π and the smallest non-zero wave-vector has a norm of one.

3.2 Initial conditions

We use two types of initial conditions, corresponding to two different situations for the magnetic and cross-helicities.

In the first case, the three lowest non-zero wave numbers of both the velocity and the magnetic field are initially loaded with a superposition of different Arnol'd-Beltrami-Childress [ABC, see Dombre et al., 1986] flows

$$(u_x, u_y, u_z) = (A \sin(kz) + C \cos(ky), B \sin(kx) + A \cos(kz), C \sin(ky) + B \cos(kx)). \quad (6)$$

Different values of the coefficients A, B, C are chosen for the first three wave numbers from a uniform random number generator. In higher wave numbers a random field with energy spectrum

$$E(k) = C_E k^{-3} \exp(-2(k/k_c)^2), \quad k_c = 3 \quad (7)$$

is superposed. The phases are chosen from a uniform random number generator with the same seed for all simulations.

In the second case, the large scale initial flow is the Orszag-Tang (OT) vortex

$$\begin{aligned} (u_x, u_y, u_z) &= (-2 \sin y, 2 \sin x, 0) \\ (b_x, b_y, b_z) &= (-2 \sin(2y) + \sin z, \\ &\quad 2 \sin(x) + \sin z, \sin x + \sin y) \end{aligned} \quad (8)$$

and in higher wave numbers a random velocity field with the same properties as above is superposed. In order to keep the initial value of magnetic helicity close to zero, no random magnetic field is added to the OT initial condition, in contrast to the ABC initial condition.

The compressive components of the initial velocity and magnetic fields are subtracted so that the initial condition is purely solenoidal. In all cases, the constant C_E in equation (7) is chosen such that

²<http://www.lra.ens.fr/~giorgos/ank>

#	N	L	λ	l_d	Re_λ	$Re = Re_m$	Re_a	Initial condition
1	128	2.60	1.30	0.0607	189	219	-	ABC
2	128	2.59	1.31	0.0605	210	219	-	OT
3	128	2.70	1.44	0.0390	217	219	100	ABC
4	128	2.72	1.44	0.0381	228	219	100	OT
5	256	2.46	0.94	0.0375	353	551	-	ABC
6	256	2.46	0.91	0.0389	377	551	-	OT
7	256	2.62	1.08	0.0185	412	551	100	ABC
8	256	2.66	1.09	0.0196	444	551	100	OT
9	512	2.28	0.67	0.0237	591	1374	-	ABC
10	512	2.12	0.58	0.0245	604	1374	-	OT
11	512	2.49	0.83	0.0091	756	1374	100	ABC
12	512	2.36	0.75	0.0095	750	1374	100	OT
13	512	1.84	0.58	0.0074	640	1374	10	ABC
14	512	2.80	1.00	0.0084	927	1374	10	OT

Table 1: Parameters of the simulations. N : linear resolution, L : integral length scale at the peak of dissipation (pd), λ : Taylor microscale (pd), l_d : dissipative scale (pd), Re_λ : Taylor microscale Reynolds number $U\lambda Re$ (pd), Re : kinetic Reynolds number, Re_m : magnetic Reynolds number, Re_a : AD Reynolds number.

$\langle \mathbf{u}^2 \rangle = \langle \mathbf{b}^2 \rangle = 1$, so that we start from equipartition between kinetic and magnetic energy. The energy of the initial condition fields is concentrated on large scales $k < k_c$ due to the exponential cutoff in (7).

In the case of the ABC initial condition, the non-dimensional cross-helicity

$$H_c = \frac{2\langle \mathbf{u} \cdot \mathbf{b} \rangle}{\sqrt{\langle \mathbf{u}^2 \rangle \langle \mathbf{b}^2 \rangle}}$$

is $\sim 2 \times 10^{-3}$, corresponding to a low initial correlation between the velocity field and the magnetic field. The mean magnetic helicity

$$H_m = \langle \mathbf{a} \cdot \mathbf{b} \rangle$$

where \mathbf{a} is the vector potential with $\mathbf{b} = \nabla \times \mathbf{a}$, is considerable, ~ 0.2 . In the case of the OT initial condition the non-dimensional cross-helicity is ~ 0.1 while the mean magnetic helicity is almost zero, $\sim 1 \times 10^{-9}$. Thus these two different initial conditions represent evolution under different constraints: in the ABC case, low cross-helicity and sizable magnetic helicity whereas in the OT case sizable cross-helicity but low magnetic helicity. This fact is important because in the ideal MHD limit (inviscid and non-resistive) the energy, cross-helicity and magnetic helicity are all conserved during the evolution. If AD is included in the ideal MHD equations, the conservation of magnetic helicity remains while energy and cross-helicity conservation are broken. This is a consequence of the form of the AD term in the induction equation, which takes the form of an advection term

$$\nabla \times (\mathbf{u}_d \times \mathbf{b}), \quad \text{with } \mathbf{u}_d = Re_a^{-1}(\mathbf{j} \times \mathbf{b})$$

the non-dimensional ion-neutral drift velocity. This form also implies that although AD is a dissipative process, it conserves magnetic flux and is thus unable to reconnect field lines.

3.3 Parameters

The parameters of the simulations performed are shown in table 1. Throughout this paper, we focus mainly on the analysis of the OT initial condition with $Re_a = 10, 100, \infty$, and we discuss the differences with respect to the ABC initial conditions only when they arise. The Taylor microscale Reynolds number Re_λ is defined as $Re_\lambda = U\lambda Re$ where $U = \sqrt{\langle \mathbf{u}^2 \rangle}$ is the r.m.s. velocity and

$$\lambda = 2\pi \left(\frac{\int_0^\infty e(k) dk}{\int_0^\infty k^2 e(k) dk} \right)^{\frac{1}{2}}$$

is the Taylor microscale, with $\int_0^\infty e(k) dk = \frac{1}{2} \langle \mathbf{u}^2 + \mathbf{b}^2 \rangle$ the total energy and $e(k)$ the total energy spectrum. The value of Re_λ is given at the peak of viscous plus Ohmic dissipation where

$$\begin{aligned} \langle \varepsilon \rangle &= \langle \varepsilon_o \rangle + \langle \varepsilon_v \rangle \\ \varepsilon_o &= Re_m^{-1} \mathbf{j}^2 \\ \varepsilon_v &= \frac{Re^{-1}}{2} \sum_{i,j=1}^3 (\partial_i u_j + \partial_j u_i)^2. \end{aligned}$$

The time when the peak of dissipation occurs is appropriate for analysis because for a given integral length scale

$$L = 2\pi \frac{\int_0^\infty k^{-1} e(k) dk}{\int_0^\infty e(k) dk} \quad (9)$$

and dissipative scale (assuming Kolmogorov scaling)

$$l_d = \left(\frac{Re^{-3}}{\langle \varepsilon \rangle} \right)^{\frac{1}{4}} \quad (10)$$

the scale separation L/l_d between the energy-containing scales and the dissipative scales is maximum. Another desirable property at the peak of dissipation is quasi-stationarity, due to the time derivative of the dissipation rate which cancels at the peak, by definition. In all the MHD simulations (with $Re_a^{-1} = 0$), two snapshots of the fields were recorded for analysis: one at the peak of dissipation and a second one one eddy turnover time later. We define the macroscopic eddy turnover time as

$$T = \sqrt{3} \frac{L}{U} \quad (11)$$

where the one-directional r.m.s. velocity $U/\sqrt{3}$ and the integral length scale L were both computed at dissipation peak to estimate when to output the next snapshot. For the AD simulations (with $Re_a^{-1} > 0$), we could not afford to compute beyond the dissipation peak.

3.4 Power-spectra

The kinetic and magnetic energy spectra of the high resolution OT runs 10-12-14 are shown in Figure 1, at the temporal peak of dissipation. The spectra are compensated by the Kolmogorov law $k^{-5/3}$ and normalized by U^2 . The extent of the inertial range, as defined by the portion of the spectra that has slope $-5/3$ is very limited, especially in the cases with AD. In the same Figure we show the limits of the inertial and dissipation ranges assumed for the analysis of section 5.2: they are taken from Uritsky et al. [2010] as $[0.21, 1.3]$ and $[0.025, 0.18]$ respectively (in units of l_0).

The kinetic and the magnetic energy appear to remain in approximate equipartition across all scales except for the smallest scales in the AD runs where magnetic energy dominates the kinetic energy (the tick-marks on the vertical lines can guide the eye to estimate the relative position of the curves between the upper and the bottom panel).

The vertical dash-dotted lines with square symbols correspond to the wave-number k_a defined in equation (5), for the cases of runs 12 and 14. Surprisingly, departures from MHD spectra start at about the same wave number for all AD runs (in the range $k \sim 5 - 8$ for both the kinetic energy spectrum and the magnetic one): this hints at the fact that $\ell_a = 2\pi/k_a$ is not the proper scale to assess the dynamical importance of AD in our simulations. In particular, dynamics can be affected at scales much larger than that in run 12. Although the difference between the pure MHD and AD MHD spectra is modest, there is a clear tendency for AD to flatten the energy spectra, especially for the magnetic energy. This is in line with the idea by Brandenburg and Zweibel [1994] that AD diffuses magnetic fields on the one hand, but on the other hand helps to build sharper magnetic structures in specific places.

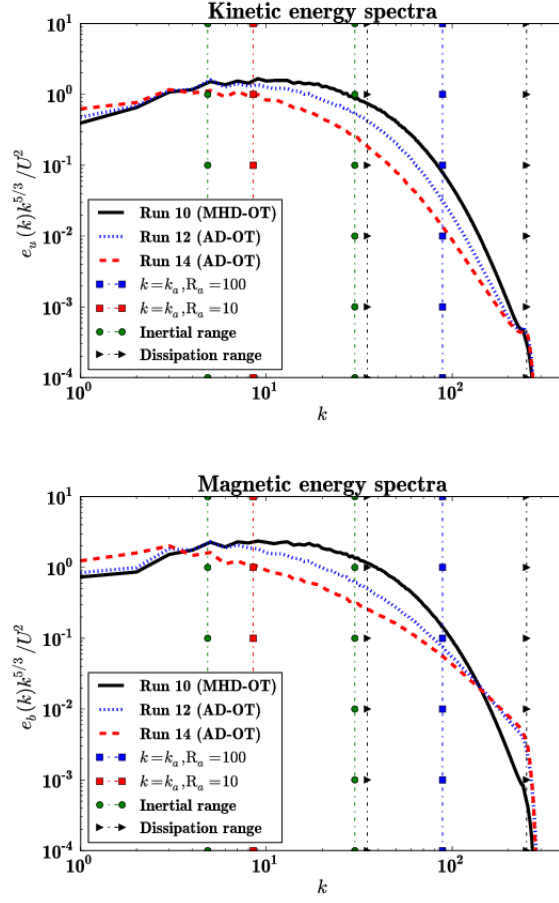


Figure 1: Compensated kinetic (top) and magnetic (bottom) energy spectra for OT runs 10, 12 and 14 at the temporal peak of dissipation. The assumed limits of the inertial and dissipation ranges are shown in dashed vertical lines. The vertical blue and red dashed-dotted lines with square symbols correspond to the expected AD critical wavenumber k_a (see equation (5)) in runs 12 and 14, respectively.

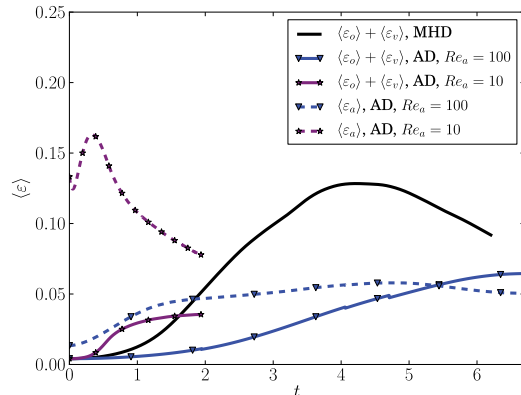


Figure 2: Time evolution of volume integrated dissipation rates for the OT runs 10, 12 and 14. Solid lines show the Ohmic plus viscous dissipation which we use to define peak dissipation.

4 The dissipation field

4.1 Total dissipation

We present in Figure 2 the time evolution of volume integrated dissipation rates. The viscous and Ohmic dissipation rates follow each other closely and we don't separate their respective contributions in this figure. Most of the time, the total dissipation rates due to viscosity, resistivity and AD are of comparable magnitude. But the total AD dissipation rate is seen to peak before the Ohmic plus viscous dissipation rate, especially at low values of Re_a . This makes our choice of the temporal peak of Ohmic plus viscous dissipation more appropriate to avoid the initial transient spike of AD dissipation (this spike is even more pronounced in the ABC case run 13).

We note that Ohmic dissipation is not enhanced by the presence of AD. On the contrary, the peak value of the Ohmic plus viscous dissipation decreases as Re_a is decreased. Even though Brandenburg and Zweibel [1994]'s idea that AD sharpens magnetic structures at small scales is valid in our simulations, AD also smooths the fields at intermediate scales and the net effect on the global Ohmic heating is to decrease it. However, this may be due to the finite dynamical range in our simulations. Higher Re_m Reynolds number simulations, if they yield enhanced magnetic power in a more extended range at small scales, could result in a globally enhanced rate of reconnection, in agreement with Zweibel and Brandenburg [1997]'s model.

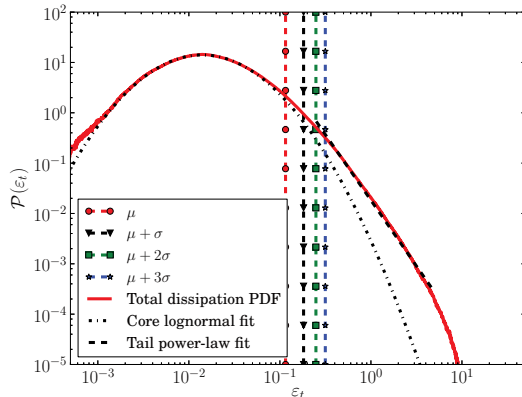


Figure 3: Log-normal core and power-law tail fit for the pdf of the total dissipation (Run 12 AD - OT). The core follows a log-normal distribution with mean $\mu_l \simeq -4.27$ and standard deviation $\sigma_l \simeq 1.03$ while the tail follows a power-law with exponent $-\tau \simeq -2.61$. Vertical lines show the mean value (red) and thresholds located at 1 (black), 2 (green) and 3 (blue) standard deviations above the mean value.

4.2 Probability distribution function

The probability density function (pdf) of the total dissipation rate

$$\varepsilon_t = \varepsilon_o + \varepsilon_v + \varepsilon_a$$

where

$$\varepsilon_a = Re_a^{-1} (\mathbf{j} \times \mathbf{b})^2$$

is shown in Figure 3 for the high-resolution run 12. The core of the pdf is very close to the log-normal distribution

$$\mathcal{P}_c(\varepsilon_t) \propto \exp\left(-\frac{(\ln \varepsilon_t - \mu_l)^2}{\sigma_l^2}\right)$$

with mean $\mu_l \simeq -4.27$ and standard deviation $\sigma_l \simeq 1.03$, while the tail of the distribution can be fitted by a power-law

$$\mathcal{P}_t(\varepsilon_t) \propto \varepsilon_t^{-\tau}$$

with exponent $\tau \simeq 2.61$. This power-law is one of the signatures of intermittency of dissipation [Frisch, 1995]. For still higher values of the total dissipation the pdf has an exponential cut-off, although these high dissipation values are close to the sampling limit. In the analysis of the next section (extraction of structures of high dissipation) effectively only the power-law range of the distribution is sampled.

In Figure 4 we present the cumulative probability density function of the total dissipation for run 12. It flattens out before reaching unity, which shows that high values of the dissipation are concentrated in

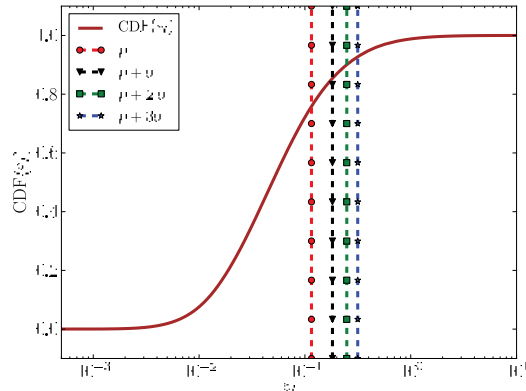


Figure 4: Cumulative probability density function of the total dissipation for run 12 (AD - OT).

a small volume subset of the spatial domain. The analysis of the next section concerns events that take place in this high-dissipation plateau.

4.3 Power-spectrum

We now investigate the distribution of the energy dissipation with respect to spatial scale. This can be discerned thanks to the power spectra of the dissipation fields, displayed in figure 5. The AD heating peaks at larger scales in comparison to Ohmic and viscous dissipation. The scale of this peak ℓ_a^* is actually only a few times smaller than the integral length scale. At this range of scales AD dissipation is much more important than Ohmic and viscous dissipation. This suggests that the heating due to AD has a characteristic length scale ℓ_a^* , which can be much larger than the dimensional estimate $\ell_a = 2\pi/k_a$ (5) for run 11. This length scale is relevant to the heating, and hence may manifest itself in structures revealed by chemical tracers of the warm chemistry of the ISM.

The AD dissipation term, $Re_a^{-1}(\mathbf{j} \times \mathbf{b})^2$, is proportional to the square of the Lorentz force. It is hence interesting to look at the influence of AD on the characteristics of the Lorentz force, in comparison with the pure MHD case. Figure 6 shows the spectrum of the Lorentz force for OT runs 10, 12 and 14. The inclusion of AD has a significant effect on the total power of the Lorentz force, reducing it importantly especially in the dissipative range. By contrast, as seen on figure 1, AD results in a deficit in the magnetic energy spectrum (and hence the spectrum of the current vector) which is much smaller in comparison to the deficit of the cross-product of these two vectors (the Lorentz force), and is only present on intermediate scales.

This is explained if AD has the effect of aligning the vectors \mathbf{j} and \mathbf{b} [as was also found in the simulations of Brandenburg et al., 1995], with a stronger effect at small scales. To put it in an other way, AD leads the magnetic field at small scales closer to a Lorentz force free configuration, where the

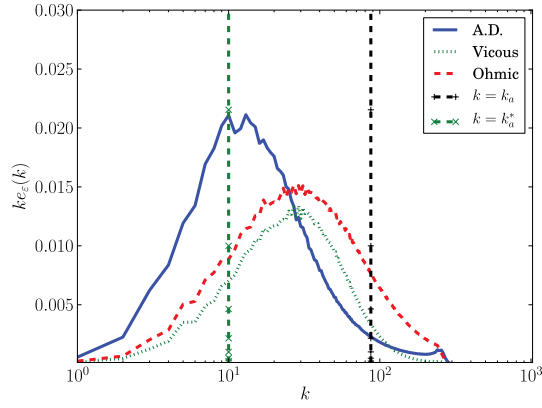


Figure 5: Compensated dissipation spectra for run 12 (AD-OT, $Re_a = 100$). Blue solid line: AD dissipation, red dashed line: Ohmic dissipation, green dotted line: viscous dissipation. We plot $k\epsilon_\epsilon(k)$ in a log-lin plot, so that the area under the curve over any interval shows directly the amount of power inside this interval. We mark the position of the maximum value of $k\epsilon_\epsilon$, at $k = k_a^* = 2\pi/\ell_a^*$, and the position of $k = k_a$.

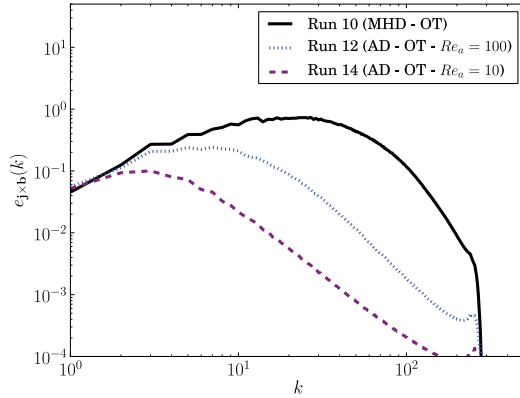


Figure 6: Power spectra of $\mathbf{j} \times \mathbf{b}$ for high resolution runs 10,12 and 14. The field becomes force-free at small scales when the strength of the AD is increased.

feedback of the magnetic field evolution on the velocity field dynamics is weaker than for MHD. This was also found in the simulations by Brandenburg and Zweibel [1995].

Here we attempt to trace this tendency back to the evolution equations. We write \mathbf{j}_\perp the component of the current vector \mathbf{j} : the double cross-product $(\mathbf{j} \times \mathbf{b}) \times \mathbf{b}$ can then be simply written $b^2 \mathbf{j}_\perp$. This allows to write

$$(\partial_t \mathbf{j})_{\text{withAD}} = (\partial_t \mathbf{j})_{\text{withoutAD}} + \nabla \times [\nabla \times (Re_a^{-1} b^2 \mathbf{j}_\perp)] \quad (12)$$

which shows that in regions where b^2 is smooth enough, the effect of AD is to diffuse out the component of the current perpendicular to \mathbf{b} , and it does so faster at small scales like any diffusion process. Hence AD brings the field closer to a force-free state, more efficiently at small scales, except perhaps at the smallest scales where b^2 varies and the behavior of equation (12) is less easy to predict.

4.4 Spatial structure

Next, we consider qualitatively the different contributions to the bulk of the dissipation field. For this purpose, each different mechanism of dissipation (Ohmic, viscous and ambipolar diffusion) is assigned to a color channel: Ohmic dissipation is assigned to the red channel, viscous dissipation to the green channel and AD dissipation to the blue channel. To emphasize the structures in the bulk of the dissipation we first compute the total dissipation value ε_l below which 10% of the heating occurs and the value ε_u below which 90% of the dissipation occurs. We discard the pixels with total dissipation $\varepsilon_t < \varepsilon_l$, we saturate the intensity of the pixels with $\varepsilon_t > \varepsilon_u$ (while keeping their intrinsic color) and we apply a logarithmic scaling for the intensity in between these two thresholds. The color of each channel is hence given by the

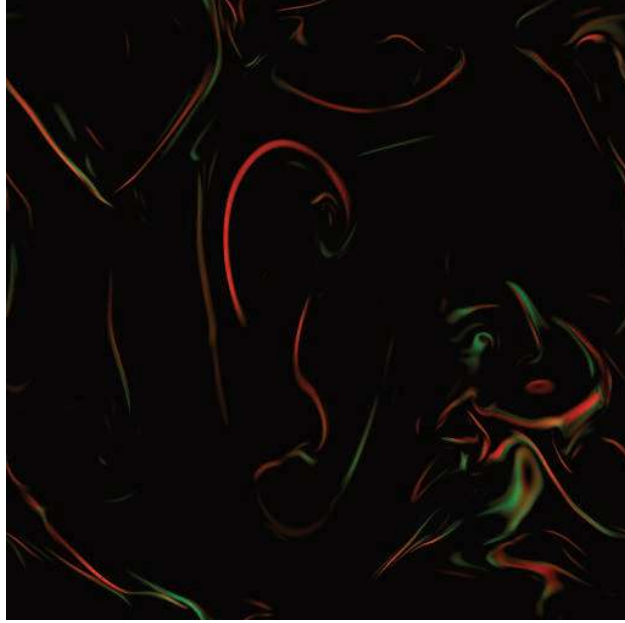


Figure 7: Color maps of a slice of the dissipation fields, run 10 (MHD - OT). Red: Ohmic dissipation, green: viscous dissipation. All snapshots are taken at the peak of dissipation.

ratio of each type of dissipation to the total dissipation

$$\begin{aligned} \text{Red} &= \frac{\varepsilon_o}{\varepsilon_t} I \\ \text{Green} &= \frac{\varepsilon_v}{\varepsilon_t} I \\ \text{Blue} &= \frac{\varepsilon_a}{\varepsilon_t} I \end{aligned}$$

with the intensity I given by

$$I = \begin{cases} 0 & \text{if } \varepsilon_t < \varepsilon_l \\ \frac{\log(\varepsilon_t) - \log(\varepsilon_l)}{\log(\varepsilon_u) - \log(\varepsilon_l)} & \text{if } \varepsilon_l \leq \varepsilon_t \leq \varepsilon_u \\ 1 & \text{if } \varepsilon_u < \varepsilon_t \end{cases}$$

The color maps of a slice through the dissipation fields are shown in figures 7-9 for all high-resolution runs with the ABC initial conditions.

In the pure MHD case (Figure 7), viscous and Ohmic dissipation are in general concentrated on thin sheets: a slice by slice inspection of the full cube reveals continuously evolving filaments at the intersection between the sheets and the plane of the slice. The length of the sheets is comparable to the integral length scale (9) while their thickness is comparable to the dissipation scale (10).

The case of AD MHD (figures 8,9) is similar in the sense that viscous and Ohmic dissipation are again concentrated on thin current sheets, although these sheets are fewer in number (more connected), and the voids of low dissipation between them are smaller. AD dissipation is significantly more diffuse than both Ohmic and viscous dissipation, and is concentrated on much thicker structures. The thickness of the AD dissipation structures seems to coincide with the AD heating length ℓ_a^* measured on the power spectra. In some cases the structures of strong AD dissipation are seen to surround the sheets of Ohmic or viscous dissipation: AD sandwiches Ohmic dissipation, much like in the Brandenburg and Zweibel [1994] picture. This is probably also seen on the left panel of Figure 7 of Padoan et al. [2000] where the structures of AD dissipation often go in pairs, except Ohmic dissipation is absent from their simulations, so reconnection proceeds only through numerical truncation errors. Between figure 7 and Figure 8, there

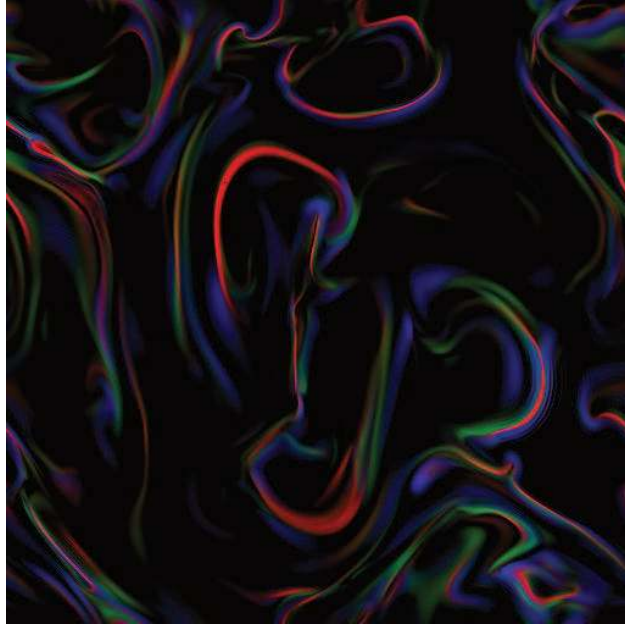


Figure 8: Same as Figure 7, Run 12, (AD - OT, $Re_a = 100$) with blue: ambipolar diffusion heating.

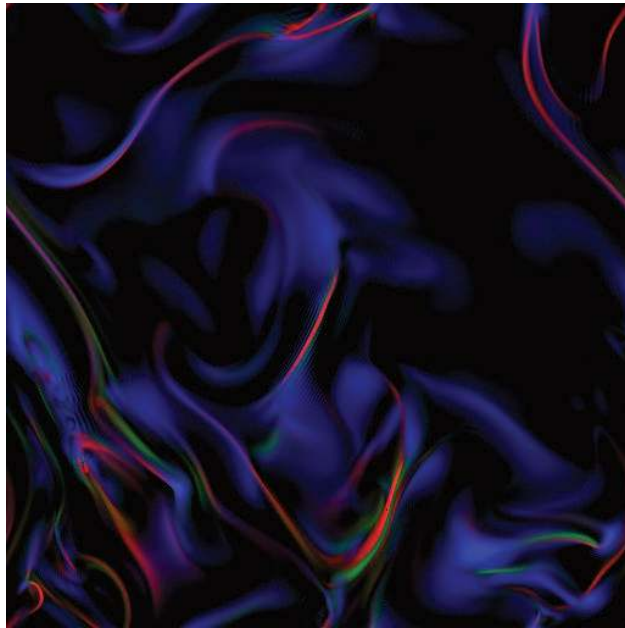


Figure 9: Same as Figure 7, Run 14, (AD - OT, $Re_a = 10$)

is little difference in the spatial structure of the dissipation field, with similar size, shape and position for each sheets of dissipation.

The above color maps reveal only a small fraction of the pixels have mixed colors (such as cyan, yellow or purple). This suggests that the dissipative structures of different nature (Ohmic, viscous or AD) are well separated.

5 Intermittency and structures of high dissipation

5.1 Structure functions

Figures 7-9 suggest that the dissipation field is not smoothly distributed in space, but is characterized by a high degree of intermittency with regions of extreme dissipation values alternating with relatively quiescent regions. The intermittent distribution of the energy dissipation rate is expected to have an impact on the structure functions of the velocity and the magnetic field. A longitudinal velocity structure function of order p is the p -th moment of the longitudinal increment of the velocity field

$$S_p^u(r) = \langle (\delta u_{\parallel}(r))^p \rangle, \quad \delta u_{\parallel}(r) = (\mathbf{u}(\mathbf{x} + \mathbf{r}) - \mathbf{u}(\mathbf{x})) \cdot \hat{\mathbf{r}}$$

where $\hat{\mathbf{r}}$ is the unit vector in the direction of \mathbf{r} . The definition for the structure function of the magnetic field $S_p^b(r)$ is completely analogous. According to standard Kolmogorov [1941] phenomenology (hereafter K41), in the inertial range the structure functions exhibit power-law scaling

$$S_p^u(r) \propto r^{\zeta_p^u}, \quad l_d \ll r \ll L$$

where the exponents ζ_p^u vary linearly with p , $\zeta_p^u = p/3$. Intermittency considerations [Frisch, 1995] lead to deviations from the linear K41 prediction. A particularly successful model of intermittency that was introduced for hydrodynamic turbulence by She and Leveque [1994] and generalized for MHD turbulence by Politano and Pouquet [1995] predicts

$$\zeta_p^{GSL}(g, C) = \frac{p}{g} \left(1 - \frac{2}{g}\right) + C \left(1 - \left(1 - \frac{2}{gC}\right)\right)^{\frac{p}{g}}$$

where g is the inverse of the inertial range scaling exponent of the velocity increment

$$\delta u_{\parallel}(r) \propto r^{1/g}$$

and C is the co-dimension of the dissipative structures, $C = 2$ for filaments and $C = 1$ for sheets in three space dimensions. K41 phenomenology predicts $g = 3$, while Iroshnikov-Kraichnan (IK) MHD phenomenology [Iroshnikov, 1964, Kraichnan, 1965] predicts $g = 4$.

In order to estimate the structure function exponents from numerical data, we used the extended self-similarity (ESS) method introduced by Benzi et al. [1993]. The exponents were estimated by computing the logarithmic slope

$$\zeta_p^u = \frac{d \log S_p^u(r)}{d \log S_*(r)}$$

where $S_*(r)$ is a structure function whose scaling behavior is known from theory. In the case of MHD turbulence, $S_*(r)$ is given by the two functions

$$S_z^{\pm}(r) = \langle \delta z_{\parallel}^{\mp} (\delta \mathbf{z}^{\pm})^2 \rangle$$

where $\delta \mathbf{z}^{\pm}$ is the increment of the Elsässer fields $\mathbf{z}^{\pm} = \mathbf{u} \pm \mathbf{b}$. Starting from the MHD equations and assuming statistical homogeneity, isotropy and stationarity, one can derive analytically

$$S_z^{\pm}(r) = -\frac{4}{3} \langle \varepsilon^{\pm} \rangle r \quad l_d \ll r \ll L \quad (13)$$

where ε^{\pm} are the dissipation rates of $(\mathbf{z}^{\pm})^2$ [Politano and Pouquet, 1998]. The linear scaling of $S_z^{\pm}(r)$ in the inertial range is confirmed approximately by the flattening seen in Figure 10 which shows compensated plots. Although the derivation of the law (13) is not proven in the case of AD MHD, the linear scaling of $S_z^{\pm}(r)$ with r is not further from linearity in comparison to pure MHD.

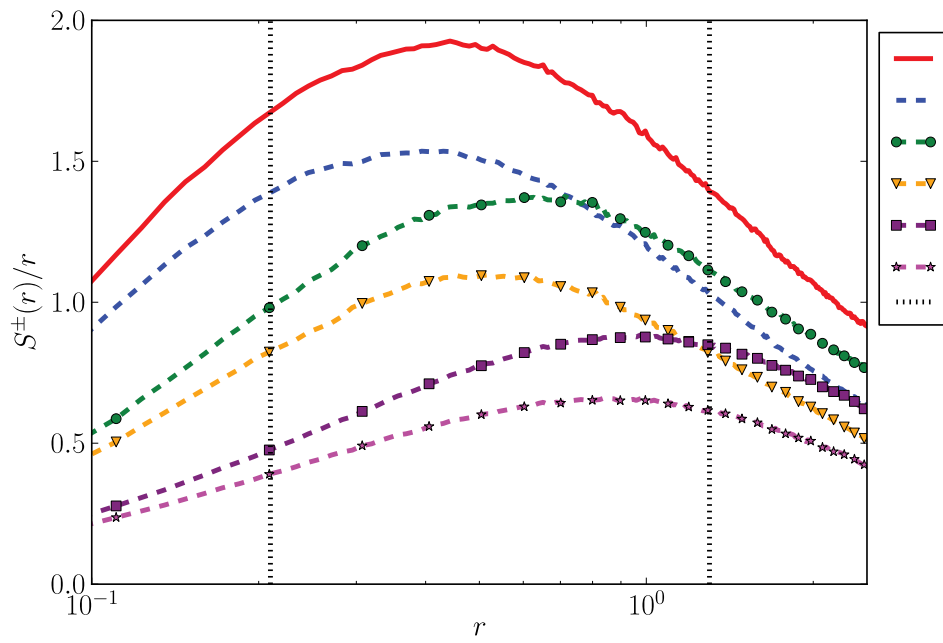


Figure 10: Compensated plot $S_z^\pm(r)/r$ for the OT runs 10,12 and 14.

The velocity and magnetic field structure function exponents up to order 8, calculated for high resolution runs 9-14 using extended self-similarity are shown in figures 11-14. We see a departure from the linear prediction of K41, a sign of intermittency, especially in the case of the magnetic field. The structure function exponents follow closely, but not exactly, the predictions of the generalized She & Levêque model with a scaling parameter $g = 3$ and a co-dimension for the structures of high dissipation around $C = 1$ (with exceptions at $C = 2$ and some below $C = 1$). This fact suggests that in the inertial range $\delta u(r)$ and $\delta b(r)$ are proportional to $r^{1/3}$, which is the prediction of K41 phenomenology, rather than $r^{1/4}$ as predicted by IK phenomenology. The value $C = 1$ of the co-dimension suggests that the structures of high dissipation in the inertial range are sheet-like, in accordance with figures 7-9 and the analysis of section 5.2. The velocity exponents for runs 9, 10 and 12 hint towards $C = 2$ (filaments) and the magnetic exponents for the OT runs exhibit a greater degree of intermittency. This indicates that even though the exponents appear to follow generalized She & Levêque models, the model's phenomenology probably does not subtend the dissipation in our simulations.

The effect of AD on intermittency is not easy to discern from these scaling exponents. In the case of the ABC initial condition, the deviation from the K41 values is larger for both the velocity and the magnetic field. The situation is reversed in the case of the OT initial condition, where the pure MHD fields appear to be more intermittent.

5.2 Extraction of structures

Following Uritsky et al. [2010] (hereafter UR10), we implemented an algorithm for the extraction of structures of high dissipation. In the problem considered, there are three types of local dissipation rates: the viscous dissipation rate,

$$\varepsilon_v = \frac{Re^{-1}}{2} \sum_{i,j=1}^3 (\partial_i u_j + \partial_j u_i)^2 \quad (14)$$

the Ohmic dissipation rate

$$\varepsilon_o = Re_m^{-1} \mathbf{j}^2 = Re_m^{-1} (\nabla \times \mathbf{b})^2 \quad (15)$$

and the AD dissipation rate

$$\varepsilon_a = Re_a^{-1} (\mathbf{j} \times \mathbf{b})^2. \quad (16)$$

A structure of high dissipation is defined as a connected set of points \mathbf{x} where

$$\varepsilon(\mathbf{x}) > \langle \varepsilon \rangle + j\sigma_\varepsilon, \quad j = 1, 2 \text{ or } 3. \quad (17)$$

In the above relation, ε can be any of the three dissipation rates or the total dissipation rate $\varepsilon_t = \varepsilon_v + \varepsilon_o + \varepsilon_a$ (or $\varepsilon_t = \varepsilon_v + \varepsilon_o$ in the case AD is absent). $\langle \varepsilon \rangle$ is the spatial mean value of the dissipation rate and σ_ε its standard deviation. For example, the three thresholds we use on total dissipation for run 12 are displayed on figures 3 and 4 over the PDF and the CDF of the total dissipation.

The algorithm is capable of isolating the structures of high dissipation so that a statistical analysis of their geometric and dynamical characteristics can be performed. The extracted structures are generally sheet-like, as can be seen in figure 15, where all structures extracted from run 12 (AD - OT) whose characteristic linear sizes L_i (see below) lie in the inertial range are shown. An example of a more complex structure can be seen in Figure 16. This structure is one of the largest extracted from this dataset. It is sheet-like, with its length larger than the integral length scale (9) and its thickness is comparable to the dissipation scale (10). It is overall characterized by a high degree of geometrical complexity.

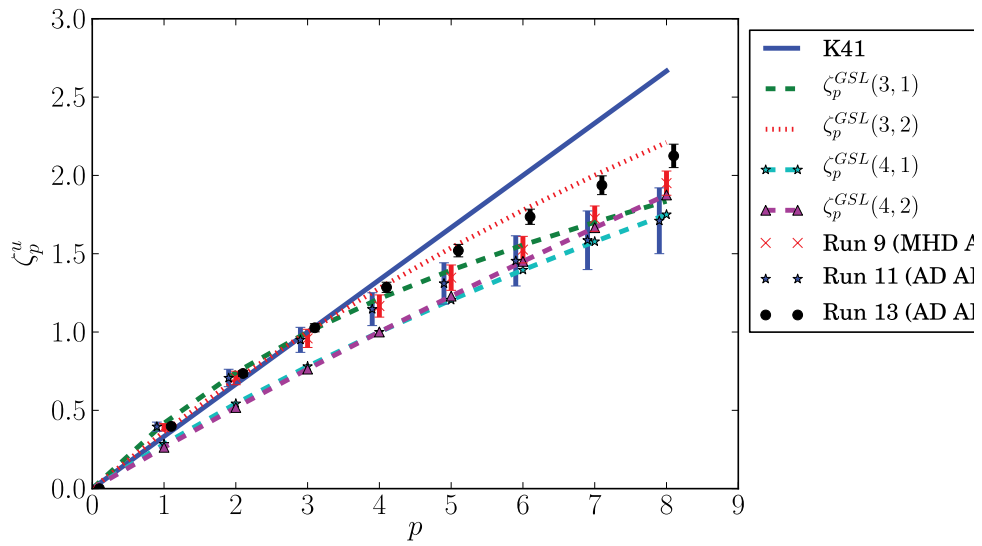


Figure 11: ESS velocity field structure function exponents for ABC runs 9-11-13.

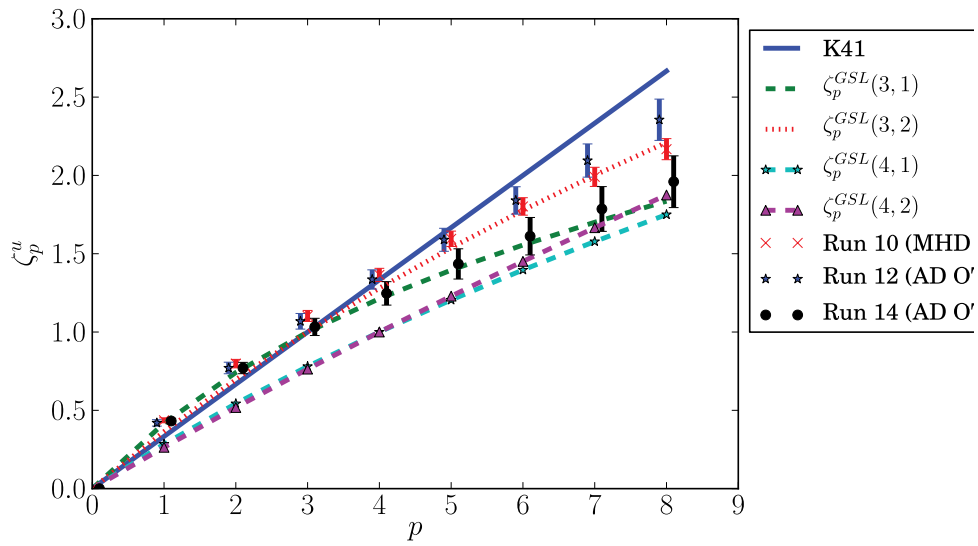


Figure 12: ESS velocity field structure function exponents for OT runs 10-12-14.

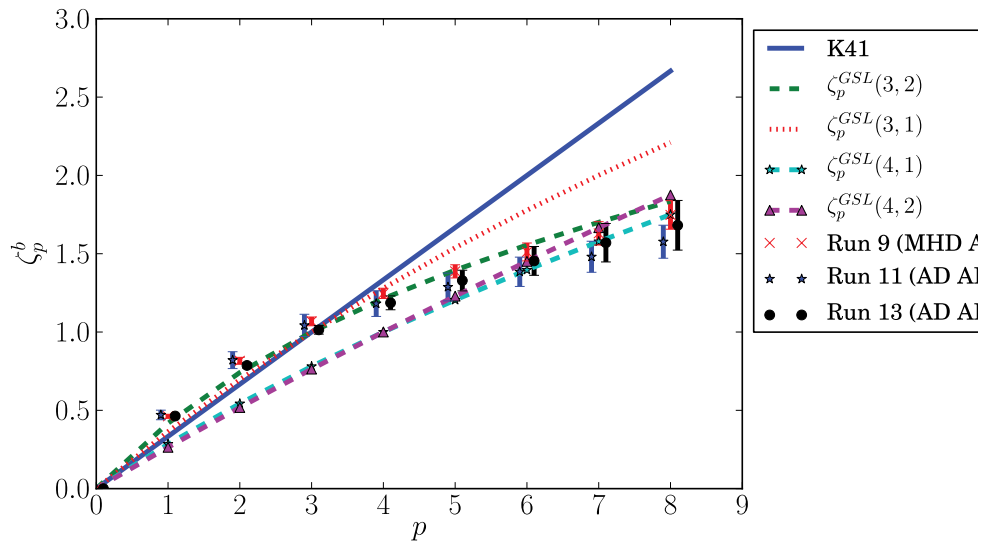


Figure 13: ESS magnetic field structure functions for ABC runs 9-11-13.

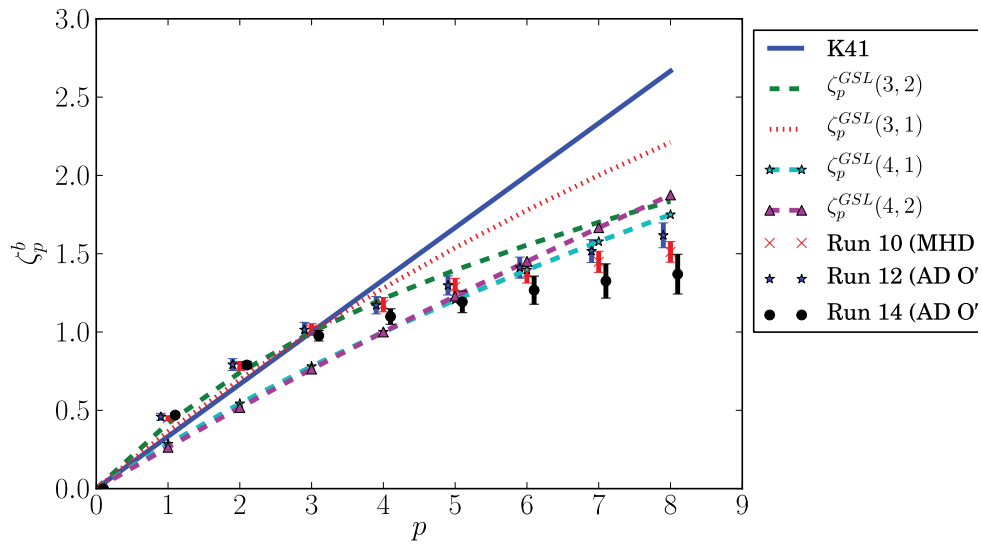


Figure 14: ESS magnetic field structure functions exponents for OT runs 10-12-14.

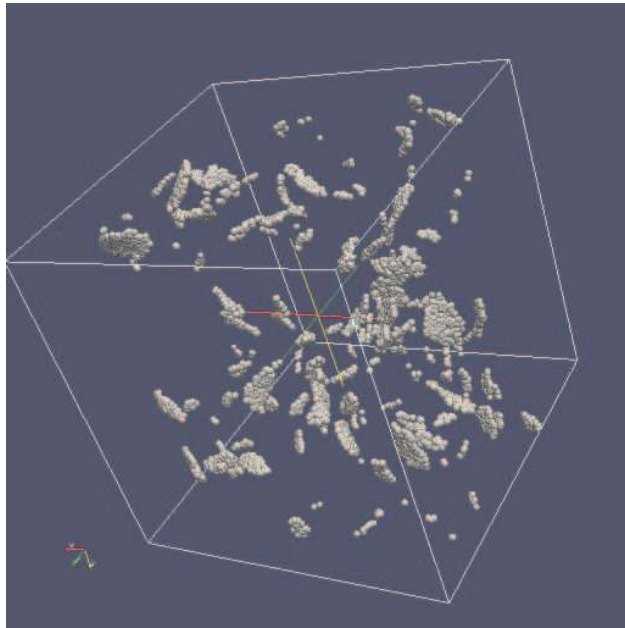


Figure 15: Inertial range structures extracted from the dataset corresponding to the peak of dissipation of Run 12 (AD - OT). They are defined as connected sets of points having values of the total dissipation three standard deviations above the mean value. Each little sphere has a 2-pixels diameter, ie: about the size of the viscous (or equivalently Ohmic) dissipation length.

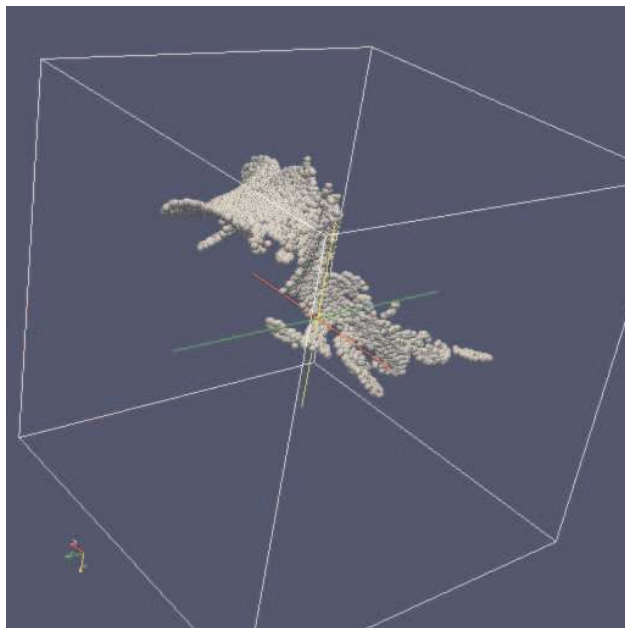


Figure 16: One of the largest structures extracted from run 12

After the extraction of the structures, the following quantities were computed for statistical analysis

$$L_i = \delta \max_{m,l \in \Lambda_i} |\mathbf{r}_m - \mathbf{r}_l| \quad (18a)$$

$$L_{\{x,y,z\}i} = \delta \max_{m,l \in \Lambda_i} |\{x,y,z\}_m - \{x,y,z\}_l| \quad (18b)$$

$$R_i = \sqrt{L_{x_i}^2 + L_{y_i}^2 + L_{z_i}^2} \quad (18c)$$

$$V_i = \delta^3 \sum_{m \in \Lambda_i} 1 \quad (18d)$$

$$A_i = \delta^2 \sum_{\substack{m \in \Lambda_i \\ M(m) \not\subset \Lambda_i}} 1 \quad (18e)$$

$$P_i = \delta^3 \sum_{m \in \Lambda_i} \varepsilon(\mathbf{r}_m) \quad (18f)$$

In the above definitions, Λ_i is the i -th structure, m its m -th point, $M(k)$ the set of 26 neighbors of the point m and $\delta = 2\pi/N$ is the grid spacing. L_i is the characteristic linear scale of the structure, $L_{\{x,y,z\}i}$ is the linear scale of its projection on the three axes, R_i is the characteristic linear scale of the smallest volume embedding the whole structure, V_i is its volume, A_i its surface and P_i the volume-integrated dissipation rate. In the next section, all statistical quantities are computed on the sample of different extracted structures. Note that the definition of R_i makes it dependent of the orientation of the structure (its value can change by tilting slightly the axis of the domain).

In order to validate our extraction procedure, we implemented it in two different ways. First, we implemented the same algorithm as UR10 (ie: recursive, using breadth-first search as explained in UR10). Second, we implemented a non-recursive algorithm: we parse the whole cube to find a pixel above threshold which is not yet included into a structure ; we tag it and we scan the whole cube several times to tag the neighboring pixels of this growing seed which happen to be above threshold, until we find no new pixel to attach to this structure ; finally we reiterate to find another pixel not yet included in a structure until we fail to find any new pixel above threshold. The second algorithm is much more CPU time consuming, but keeps the memory usage constant and is easier to implement. We checked that both algorithms identify strictly the same structures for the two implementations in the low resolution cases.

Like in UR10, all the above quantities are found to exhibit power-law scaling with respect to structure linear size L_i , with different scaling behavior in the inertial and dissipative ranges. The quantity X_i , which could be any of L_i, R_i, V_i, A_i, P_i scales as

$$X_i \propto L_i^{D_X}$$

with different scaling exponents D_X in the inertial and dissipative ranges, while the pdf of X_i scales as

$$\mathcal{P}(X_i) \propto X_i^{-\tau_X}$$

with different scaling exponents τ_X in the inertial and dissipative ranges. As an example, the scaling relations $P_i \propto L_i^{D_P}$ and $\mathcal{P}(P_i) \propto P_i^{-\tau_P}$ are shown in figures 17 for the structures extracted from Run 12 (AD - OT), at the peak of dissipation, with a threshold of two standard deviations above mean value. The limits of the inertial and dissipation ranges are also shown (as used by UR10, see section 3.4). The upper limit of the dissipation range is just below the lower limit of the inertial range, while the lower limit of the dissipation range is ~ 2 times the numerical resolution.

5.3 Comparison with UR10

In this section we compare the results of the statistical analysis of structures of high dissipation with those of UR10. These authors consider pure MHD and study the structures of high Ohmic dissipation or high enstrophy

$$\varepsilon_\omega = Re^{-1} \boldsymbol{\omega}^2, \quad \boldsymbol{\omega} = \nabla \times \mathbf{u}$$

The results for the scaling exponents are shown in figure 18, for the case of the OT initial condition. The case of the ABC initial condition (not shown) is similar. The exponents are calculated from run 10 which in terms of initial condition and Reynolds number is similar with run III of UR10. As in the

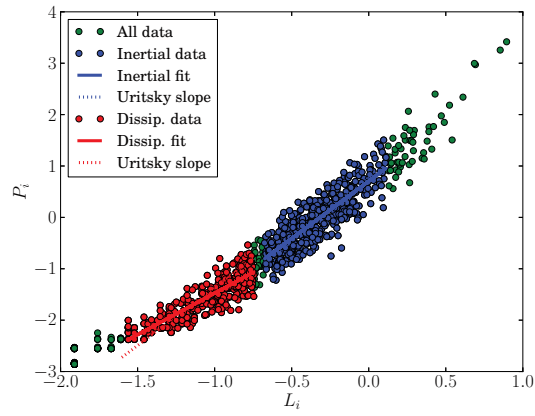


Figure 17: Scaling relations $P_i \propto L_i^{D_P}$ from Run 12 (AD - OT), at the peak of dissipation, with a threshold of two standard deviations above mean value. The dotted line shows the effect of adopting the slope found by Uritsky et al. [2010] instead of our own slope.

present paper, the snapshot analyzed is on the peak of dissipation. The structures of high dissipation are defined as connected sets of points having values of the Ohmic dissipation two standard deviations above the mean value. We keep the same definitions as UR10 for the inertial and dissipative ranges (cf. section 3.4).

Figure 18 shows that the agreement between our results and those of UR10 is not completely satisfactory. Although most three-sigma error bars are compatible and the errors are on the same order, there remains systematic differences, especially for our pdf exponents which appear to yield shallower pdfs than UR10. The least square method used by UR10 to estimate the slope of power-law pdfs is known to introduce some bias and the maximum-likelihood estimate method (MLE) should be used instead [see Clauset et al., 2009]. We computed the exponents with the MLE, and found them to be very close to our least-square values. We turned to explore the effects of some systematics due to the uncertainty on the boundaries of the inertial and dissipative range and the size of the bins used to produce the pdfs. We varied randomly these parameters with factors in an octave centered on their initial chosen values. The excursion of the resulting three-sigma error bars over a thousand of such realizations are plotted as thin red error bars on Figure 18. A slight displacement of the inertial or dissipative range boundaries incorporates (or leaves out) new data near the edge of the fitting intervals, where their leverage on the fitted slope is quite important. The resulting figure shows that such systematics can account for nearly all discrepancies with respect to UR10, except for the correlation between the total dissipation of structures and their linear size. We illustrate the corresponding discrepancy on Figure 17 where the dotted red line shows the slope followed by UR10 data: this line clearly falls below our data at small scales. This suggests that our smallest structure have a higher value of dissipation. This may perhaps be traced back to the slightly more refined dealiasing rule which we use. The picture is the same for the ABC runs, except for the error bar 0.02 on D_A in Run I of UR10 (see their Table II) which is probably a typo as the value they quote does not correspond to the scatter displayed in their Figure 3.

To validate further our results, we compared the computed scaling exponents for the dataset corresponding to the temporal peak of total dissipation of the pure MHD run with ABC or OT initial condition (Run 9 and 10) with those computed from a snapshot taken one macroscopic eddy turnover time later, in the decay period of the turbulence. In agreement with the results of UR10, we find no statistical difference between the two snapshots (one-sigma error bars are compatible). Similarly, we compared the exponent values computed based on \mathbf{j}^2 with those computed based on ω^2 for the dataset corresponding to the peak of total dissipation of the same runs (Runs 9 and 10). Again the exponents were seen to be compatible within one-sigma error bars, as in UR10.

5.4 Structures based on total dissipation

In this section we focus on the statistical analysis of structures extracted based on the total dissipation $\varepsilon_t = \varepsilon_o + \varepsilon_v + \varepsilon_a$ for both pure MHD and AD MHD. The analysis based on the total dissipation is more relevant to the heating of the ISM because all three different types of dissipation can be important heating agents. AD has an additional specificity because the ion-neutral drift increases the effective temperature of the chemical reactions, but we do not consider this yet in the present work. In the following, we will note D_X for the linear size exponents and τ_X for the probability exponents of a characteristic X . All the structures discussed in this section are defined as connected sets of points having values of the total dissipation two standard deviations above the mean value.

In Table 2 we present the results of the structure extraction algorithm. The relative amount of dissipation contained by all the detected structures does not depend much on the Reynolds number, but the volume filling factor of the structures decreases as the Reynolds number increases. The presence of AD results in fewer detected structures than without AD (except for run 13). However, they fill roughly the same volume fraction, thus AD structures tend to be larger. This difference between the number of different structures in pure MHD and AD increases with the Reynolds number. Figure 19 gives a more detailed view of the fraction of total dissipation contained in structures with a value above a given threshold as a function of the volume fraction occupied by these structures. The curve rises steeply near the origin, so that 30 percent of the dissipation is contained in less than 3 percent of the total volume. The steepness at the origin is seen to be mainly due to the Ohmic heating: this is in line with the original picture of Brandenburg and Zweibel [1994] where AD forms sharp features in which Ohmic dissipation is favored.

Figures 20 and 21 summarize all results on the exponents for the total dissipation two standard

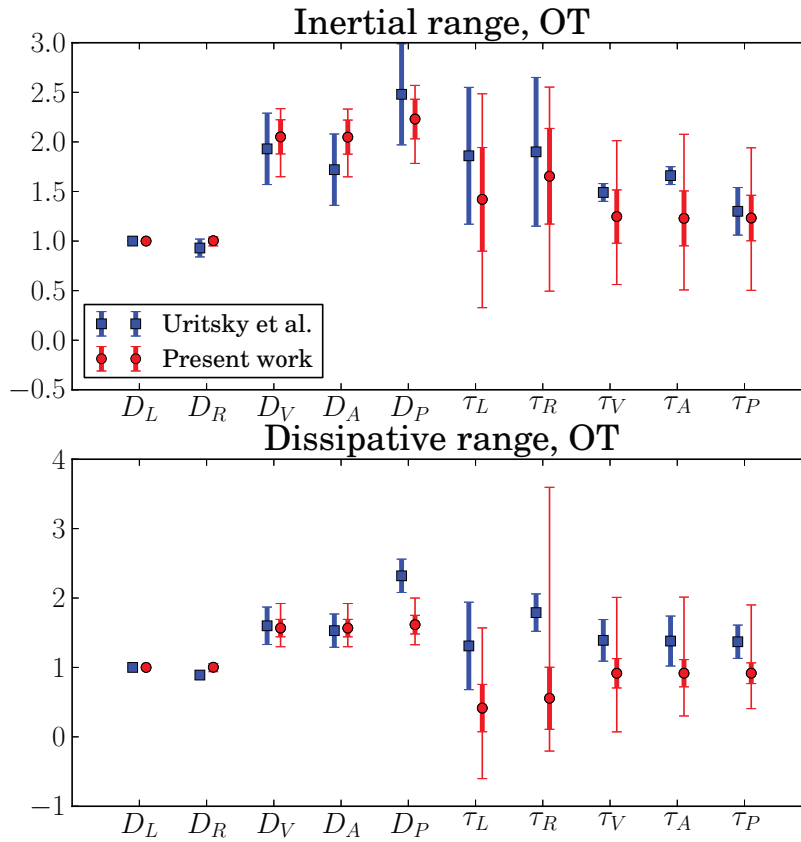


Figure 18: Scaling exponents for structures extracted based on the Ohmic dissipation (red circles), comparison with results of UR10 (blue squares). Upper panel: Inertial range exponents for our Run 10 (MHD-OT) compared with the corresponding Run III of UR10. Lower panel: Dissipative range exponents for the same runs. Thick error bars are three-sigma error brackets. Thin red error bars estimate the systematics related to the choice of the boundaries of the inertial and dissipative ranges as well as the bin size for the definition of the pdfs: see text for details.

#	N	Re_λ	Re_a	# of structures	% of volume	% of total dissipation
1	128	189	-	87	3.90	23.85
2	128	210	-	54	3.81	27.29
3	128	217	100	72	3.78	23.65
4	128	228	100	34	3.90	26.91
5	256	353	-	215	3.26	27.32
6	256	377	-	233	3.26	26.80
7	256	412	100	144	2.86	26.40
8	256	444	100	153	2.98	26.53
9	512	591	-	790	2.70	31.30
10	512	604	-	1166	2.77	30.33
11	512	756	100	375	2.17	29.21
12	512	750	100	418	2.57	29.48
13	512	640	10	1167	2.94	28.01
14	512	927	10	378	1.75	22.00

Table 2: Results of the structure extraction algorithm for all runs and structures defined as connected sets of points having a value of the total dissipation two standard deviations above mean value.

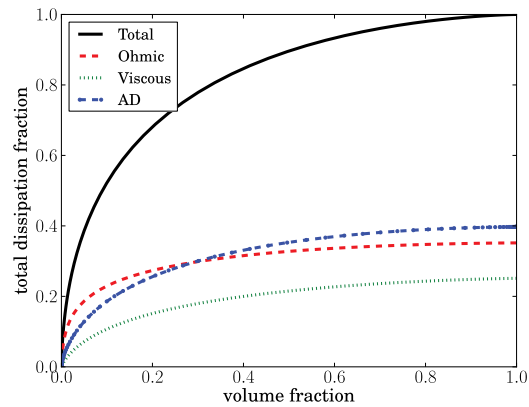


Figure 19: We look at the subset of pixels above a given threshold of total dissipation in run 12 (AD-OT, $Re_a = 100$) at the dissipation peak. For each value of the threshold, we plot the fraction of the total energy dissipation on this subset versus the volume of this subset (black curve). We also give the fraction of the total dissipation on this subset for each nature of dissipation (red: Ohmic, green: viscous, blue: AD).

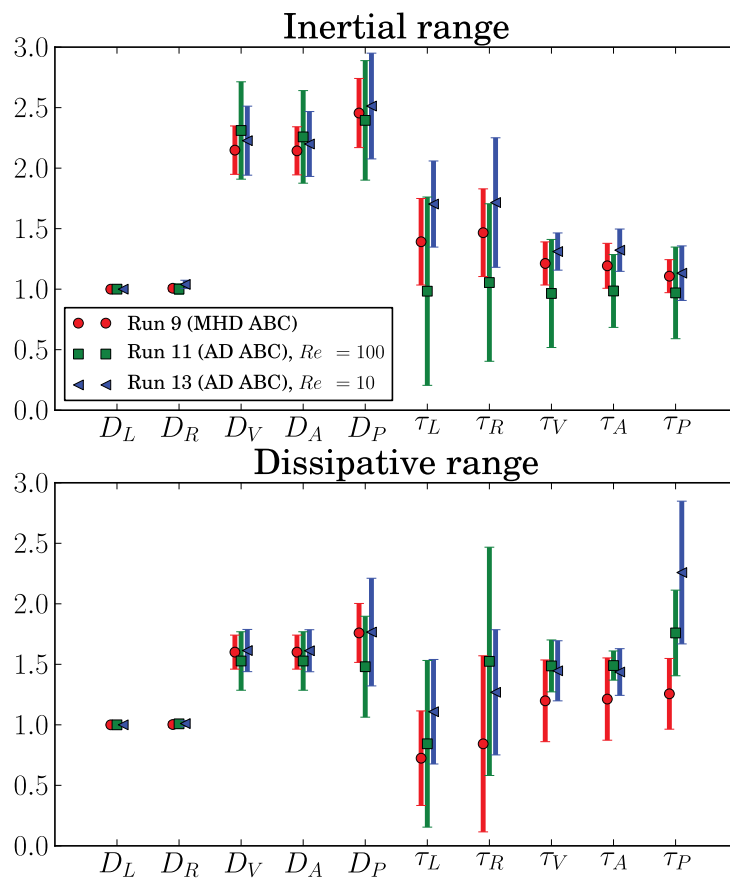


Figure 20: Comparison of scaling exponents with three-sigma error bars between pure MHD (red circles) and AD MHD (green squares $Re_a = 100$ and blue triangles $Re_a = 10$) - ABC Runs 9,11,13

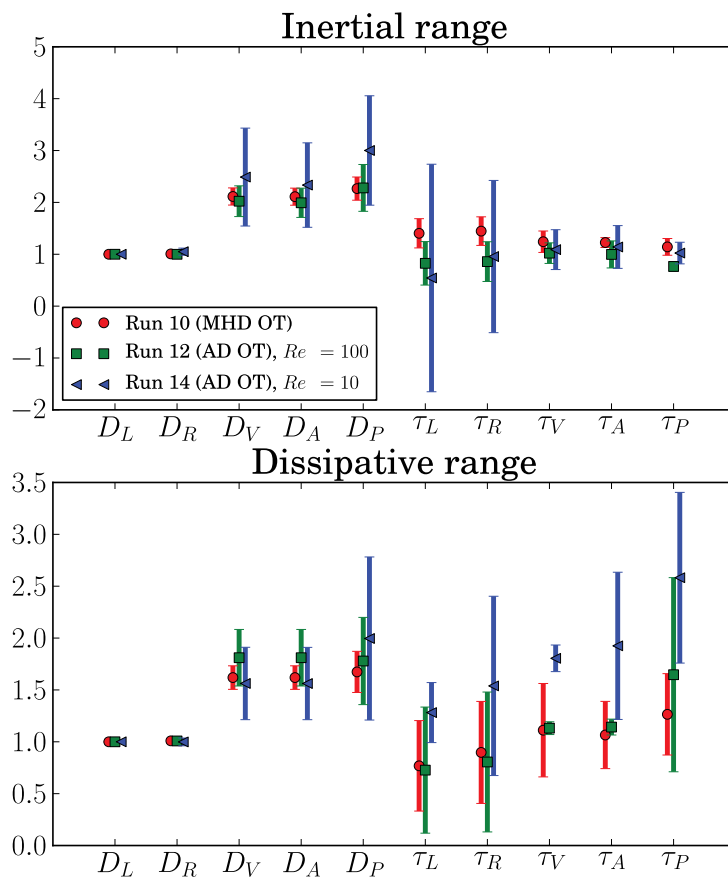


Figure 21: Same as Figure 20 but for the OT Runs 10,12,14.

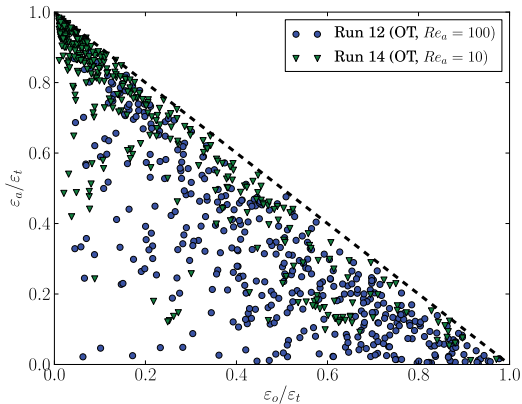


Figure 22: Scatter plots of the ratio $\varepsilon_o/\varepsilon_t$ versus the ratio $\varepsilon_a/\varepsilon_t$ for AD-OT runs 12 and 14.

deviations above the mean. Although most three-sigma error bars are compatible, in particular for the D_X exponents which are unchanged with AD, some systematic differences exist for the pdfs exponents τ_X . The pdfs exponents are in general steeper in the dissipation range: AD seems to favor more fragmented structures in the dissipative range. This confirms the tendency for more intermittency with AD that was suggested by the structure functions analysis. However, we see no clear cut tendency in the inertial range. If we discard the strong AD results ($Re_a = 10$), the inertial range shows a behavior opposite from the dissipative range (shallower pdfs slope, ie: larger structures are favored when AD is present). However if we now look only at the MHD runs and the $Re_a = 10$ runs, the inertial range sees no change in the τ_X exponents for the OT runs, but bigger exponents for the ABC runs, in agreement with the dissipative range and contrary to the $Re_a = 100$ runs...

This complicated picture might perhaps not be genuine, as the huge systematics experienced for the comparison with UR10 show. However, the dependence of the intermittency statistics on the initial conditions (seen both in the structure pdfs slopes and in the structure functions exponents) points at their difference in magnetic helicity. In the OT initial condition, the initial value of magnetic helicity is almost zero, and the equation of magnetic helicity evolution is unchanged by the inclusion of the AD term. As far as the effects of viscosity and resistivity are neglected, both the pure MHD and AD MHD solution evolve under the same constraint of zero magnetic helicity. A zero value for the magnetic helicity is an important constraint because it implies statistical reflection invariance, a property which the ABC runs will not share. In the ABC initial condition, the constraint of very low cross-helicity is broken by AD, which provides a source term in the cross-helicity equation.

The above analysis does not give any information on the relative amount of Ohmic, viscous and AD dissipation contained within each structure. To answer this question, we show in figure 22 scatter plots of the ratio of total Ohmic dissipation to total dissipation $\varepsilon_o/\varepsilon_t$ versus the ratio of total AD dissipation to total dissipation $\varepsilon_a/\varepsilon_t$ in the two OT runs 12 and 14. In all AD cases there is a tendency for the structures

to cluster close to the line of zero viscous dissipation (dashed line in figure 22). This shows that within the structures of high total dissipation, viscous dissipation is relatively less important. The relative values of Ohmic and AD dissipation span however the whole spectrum, in contrast to the impression given by our RGB slices (see figures 7 to 9): this could be a genuine difference between the extreme dissipation events and the bulk of the dissipation shown on the RGB figures, or the extraction algorithm of connected structures could merge nearby sheets with different dissipation natures. We checked on a pixel by pixel scatter plot similar to Figure 22 that it is indeed a genuine difference. For the strongest AD runs, though, the intense dissipation structures tend to be predominantly due to AD heating (top left corner in Figure 22).

6 Concluding remarks

We performed a 3D numerical study of the structures of high dissipation in MHD turbulence, with the inclusion of ambipolar diffusion. At the Reynolds numbers studied, the total dissipation due to viscosity, resistivity and AD are of comparable magnitude.

Kinetic and magnetic energy spectra show that ambipolar diffusion enhances the turbulent energy to small scales at the expense of intermediate scales. This agrees with the idea of Brandenburg and Zweibel [1994] that AD can sharpen the magnetic gradients, but the effect is not strong enough to increase the total Ohmic dissipation rate in our simulations. Previous authors Li et al. [2008] and Oishi and Mac Low [2006] have examined the case of driven two-fluids compressible turbulence with a mean magnetic field and they find different results: Oishi and Mac Low [2006] find no effect on the slope of the spectrum (for $Re_a = 2.5$ and $Re_a = 5$) while Li et al. [2008] find that AD *steepens* it, although they don't display the results for their runs with $Re_a = 12$ and $Re_a = 120$, the only ones which have ℓ_a in the computed range of scales as in our study. It should be noted that both these papers neglect Ohmic diffusion, and rely on truncation errors only to reconnect the field: the present work is the first to account for AD in the presence of controlled Ohmic and viscous dissipation. This is important because the dissipation physics can be quite different from the numerical dissipation as was demonstrated by Fromang and Papaloizou [2007], Fromang et al. [2007] in magneto-rotational turbulence.

As in Oishi and Mac Low [2006], we fail to detect a significant change of regime in the spectra at the expected AD length scale ℓ_a , but in our simulations it happens at a greater length scale. This length scale ℓ_a is predicted from the balance between the moduli of the Fourier coefficients for the inertial e.m.f. and the AD e.m.f.. We would underestimate ℓ_a if AD was more coherent in time than the advection of the field, and so we conjecture that AD terms have a greater coherence time than the inertial terms.

In our simulations, we observe that AD shuts off the Lorentz force at small scales: this shifts the peak of the AD heating power spectrum to larger scales. The position of that peak defines a scale which seems to match the characteristic thickness of the sheets where AD heating is strong. This scale ℓ_a^* might be revealed by the characteristic chemistry of AD heating where neutral-ion endothermic reactions are favored (e.g.: CH^+ or SH^+ formation, see Godard et al., 2009). Table 3 sums up the characteristics of various environments of the ISM. We identify the integral length scale and the r.m.s. velocity in our simulations to their corresponding physical values in each considered ISM components to apply our results. Although we find that Re_a^{-1} in the ISM varies from 10^{-3} to 10^{-2} , we use $\ell_a^* = 0.6$ as measured in our AD simulations with $Re_a^{-1} = 0.01$ to estimate the scale $l_0 \ell_a^*$ of the AD diffusion heating. The AD dissipation heating is always about a fourth of the typical scale whereas $l_0 \ell_a$ can be much smaller.

The qualitative picture of the dissipation field suggests that it is dominated by intermittent sheet-like structures which alternate with large voids of low dissipation. The sheets of various dissipative nature (Ohmic, viscous or AD) appear to be clearly separated, except for the highest dissipation rates, where viscosity fades out and Ohmic and AD heating blend. AD heating sheets are often seen to sandwich much thinner regions of strong Ohmic or viscous dissipation, as in the simple case studied by Brandenburg and Zweibel [1994]. The high degree of intermittency is confirmed by the computation of the structure function exponents for the velocity and the magnetic field, as well as by the pdf of the total dissipation, which exhibits a log-normal core and a strong power-law tail for high values of the dissipation. We compared the statistics of the structures of strong dissipation with those of UR10 and we obtain only marginal agreement, probably because of the systematics linked with the definition of the inertial and dissipative ranges. The statistical analysis of structures of high total dissipation reveals the highly intermittent nature of the dissipation field, as more than 30% of the dissipation takes place in less than

Table 3: Characteristics of various components of the ISM. Dimensions are recovered from our simulations by assuming $L \simeq 2.5$, $\ell_a^* \simeq 0.6$ and $u_0 \simeq \sqrt{3}.U_a$ where U_a is the line-of-sight r.m.s. Alfvén velocity. The quantity $\gamma\rho_i$ is computed by assuming the ions are essentially C^+ ions with a number density $n_i = 10^{-4}n_H$.

		CNM	molecular clouds	low-mass dense cores
Density	$n_H(\text{cm}^{-3})$	30	200	10^4
Length scale	$L.l_0$ (pc)	10	3	0.1
r.m.s. velocity	$U.u_0/\sqrt{3}$ (km/s)	3.5	1	0.1
Alfvén velocity	$U_a = u_0/\sqrt{3}$ (km/s)	3.4	2	1
AD Reynolds number	$Re_a^{-1} = 1/\gamma\rho_i/(t_0)$	$1.2 \cdot 10^{-2}$	$3.6 \cdot 10^{-3}$	$1.1 \cdot 10^{-3}$
AD heating length	$\ell_a^*.l_0$ (pc)	2.4	0.72	0.024
AD dynamical length	$\ell_a.l_0 = 2\pi l_0 Re_a^{-1}.U_a^2/U^2$ (pc)	0.28	0.10	0.026

3% of the volume. No significant difference in the scaling laws between pure MHD and AD MHD was found, but the slope of the power-law pdfs is affected in the dissipative range, with a statistical preference towards more fragmented structures.

In future work, we intend to make progress towards a more realistic picture of the ISM, relaxing the incompressible hypothesis, with the final aim of including realistic cooling. We also hope our statistical results will provide new ways to approach the observed characteristics of the ISM, intermediate between direct post-processing of 3D numerical simulations and the building of line of sights with elementary models such as shocks or vortices [Godard et al., 2009].

Acknowledgments

We thank V.M. Uritsky for sharing with us his experience with the structures extraction algorithm. We would also like to thank the MesoPSL team of the Observatoire de Paris for providing support for the numerical simulations.

References

- S. A. Balbus and C. Terquem. Linear Analysis of the Hall Effect in Protostellar Disks. *ApJ*, 552:235–247, May 2001. doi: 10.1086/320452.
- R. Benzi, S. Ciliberto, R. Tripiccion, C. Baudet, F. Massaioli, and S. Succi. Extended self-similarity in turbulent flows. *Phys. Rev. E*, 48:R29–R32, Jul 1993. doi: 10.1103/PhysRevE.48.R29.
- O. M. Blaes and S. A. Balbus. Local shear instabilities in weakly ionized, weakly magnetized disks. *ApJ*, 421:163–177, January 1994. doi: 10.1086/173634.
- A. Brandenburg and E. G. Zweibel. The formation of sharp structures by ambipolar diffusion. *ApJ*, 427:L91–L94, June 1994. doi: 10.1086/187372.
- A. Brandenburg and E. G. Zweibel. Effects of Pressure and Resistivity on the Ambipolar Diffusion Singularity: Too Little, Too Late. *ApJ*, 448:734, August 1995. doi: 10.1086/176001.
- A. Brandenburg, A. Nordlund, R. F. Stein, and U. Torkelsson. Dynamo-generated Turbulence and Large-Scale Magnetic Fields in a Keplerian Shear Flow. *ApJ*, 446:741, June 1995. doi: 10.1086/175831.
- Claudio Canuto, M Yousuff Hussaini, Alfio Quarteroni, and Thomas A Zang. *Spectral methods in fluid dynamics*. Springer-Verlag, 1988.

- A. Clauset, C. R. Shalizi, and M. E. J. Newman. Power-Law Distributions in Empirical Data. *SIAM Review*, 51:661–703, January 2009. doi: 10.1137/070710111.
- T. Dombre, U. Frisch, M. Henon, J. M. Greene, and A. M. Soward. Chaotic streamlines in the ABC flows. *Journal of Fluid Mechanics*, 167:353–391, June 1986. doi: 10.1017/S0022112086002859.
- B. T. Draine, W. G. Roberge, and A. Dalgarno. Magnetohydrodynamic shock waves in molecular clouds. *ApJ*, 264:485–507, January 1983. doi: 10.1086/160617.
- B. G. Elmegreen. Energy dissipation in clumpy magnetic clouds. *ApJ*, 299:196–210, December 1985. doi: 10.1086/163692.
- Bruce G. Elmegreen and John Scalo. Interstellar turbulence i: Observations and processes. *ARA&A*, 42(1):211–273, 2004. doi: 10.1146/annurev.astro.41.011802.094859.
- E. Falgarone and J.-L. Puget. The intermittency of turbulence in interstellar clouds: implications for the gas kinetic temperature and decoupling of heavy particles from the gas motions. *A&A*, 293:840–852, January 1995.
- D. R. Flower and G. Pineau des Forets. Non-thermal sputtering of interstellar grains in magnetohydrodynamic shocks. *MNRAS*, 275:1049–1056, August 1995.
- D. R. Flower, G. Pineau des Forets, and T. W. Hartquist. Theoretical studies of interstellar molecular shocks. I - General formulation and effects of the ion-molecule chemistry. *MNRAS*, 216:775–794, October 1985.
- U. Frisch. *Turbulence: the legacy of A. N. Kolmogorov*. Cambridge university press, 1995.
- S. Fromang and J. Papaloizou. MHD simulations of the magnetorotational instability in a shearing box with zero net flux. I. The issue of convergence. *A&A*, 476:1113–1122, December 2007. doi: 10.1051/0004-6361:20077942.
- S. Fromang, J. Papaloizou, G. Lesur, and T. Heinemann. MHD simulations of the magnetorotational instability in a shearing box with zero net flux. II. The effect of transport coefficients. *A&A*, 476:1123–1132, December 2007. doi: 10.1051/0004-6361:20077943.
- B. Godard, E. Falgarone, and G. Pineau Des Forêts. Models of turbulent dissipation regions in the diffuse interstellar medium. *A&A*, 495:847–867, March 2009. doi: 10.1051/0004-6361:200810803.
- PS Iroshnikov. Turbulence of a conducting fluid in a strong magnetic field. *Sov. Astron.*, 7:566, 1964.
- AN Kolmogorov. The local structure of turbulence in incompressible viscous fluid for very large reynolds numbers [in russian]. *Dokl. Akad. Nauk SSSR*, 30:299–303, 1941.
- Robert H. Kraichnan. Inertial-range spectrum of hydromagnetic turbulence. *Phys. Fluids*, 8(7):1385–1387, 1965. doi: 10.1063/1.1761412.
- T. Kudoh and S. Basu. Three-dimensional Simulation of Magnetized Cloud Fragmentation Induced by Nonlinear Flows and Ambipolar Diffusion. *ApJ*, 679:L97–L100, June 2008. doi: 10.1086/589618.
- T. Kudoh and S. Basu. Formation of Collapsing Cores in Subcritical Magnetic Clouds: Three-dimensional Magnetohydrodynamic Simulations with Ambipolar Diffusion. *ApJ*, 728:123, February 2011. doi: 10.1088/0004-637X/728/2/123.
- P. Lesaffre, G. Pineau des Forêts, B. Godard, P. Guillard, F. Boulanger, and E. Falgarone. Low-velocity shocks: signatures of turbulent dissipation in diffuse irradiated gas. *A&A*, 550:A106, February 2013. doi: 10.1051/0004-6361/201219928.
- P. S. Li, C. F. McKee, and R. I. Klein. The Heavy-Ion Approximation for Ambipolar Diffusion Calculations for Weakly Ionized Plasmas. *ApJ*, 653:1280–1291, December 2006. doi: 10.1086/508977.

- P. S. Li, C. F. McKee, R. I. Klein, and R. T. Fisher. Sub-Alfvénic Nonideal MHD Turbulence Simulations with Ambipolar Diffusion. I. Turbulence Statistics. *ApJ*, 684:380–394, September 2008. doi: 10.1086/589874.
- P. S. Li, C. F. McKee, and R. I. Klein. Sub-Alfvénic Non-ideal Magnetohydrodynamic Turbulence Simulations with Ambipolar Diffusion. III. Implications for Observations and Turbulent Enhancement. *ApJ*, 744:73, January 2012. doi: 10.1088/0004-637X/744/1/73.
- Pak Shing Li, Andrew Myers, and Christopher F. McKee. Ambipolar diffusion heating in turbulent systems. *ApJ*, 760(1):33, 2012.
- M.-M. Mac Low, M. L. Norman, A. Konigl, and M. Wardle. Incorporation of ambipolar diffusion into the ZEUS magnetohydrodynamics code. *ApJ*, 442:726–735, April 1995. doi: 10.1086/175477.
- J. Masson, R. Teyssier, C. Mulet-Marquis, P. Hennebelle, and G. Chabrier. Incorporating Ambipolar and Ohmic Diffusion in the AMR MHD Code RAMSES. *ApJS*, 201:24, August 2012. doi: 10.1088/0067-0049/201/2/24.
- C. F. McKee, P. S. Li, and R. I. Klein. Sub-Alfvénic Non-ideal MHD Turbulence Simulations with Ambipolar Diffusion. II. Comparison with Observation, Clump Properties, and Scaling to Physical Units. *ApJ*, 720:1612–1634, September 2010. doi: 10.1088/0004-637X/720/2/1612.
- L. Mestel and L. Spitzer, Jr. Star formation in magnetic dust clouds. *MNRAS*, 116:503, 1956.
- L. Monchick and J. Schaefer. Theoretical studies of H₂-H₂ collisions. II. Scattering and transport cross sections of hydrogen at low energies: Tests of a new ab initio vibrotor potential. *J. Chem. Phys.*, 73: 6153–6161, December 1980. doi: 10.1063/1.440107.
- D. J. Mullan. The structure of transverse hydromagnetic shocks in regions of low ionization. *MNRAS*, 153:145, 1971.
- F. Nakamura and Z.-Y. Li. Quiescent Cores and the Efficiency of Turbulence-accelerated, Magnetically Regulated Star Formation. *ApJ*, 631:411–428, September 2005. doi: 10.1086/432606.
- M. Nakamura, I. L. Tregillis, H. Li, and S. Li. A Numerical Model of Hercules A by Magnetic Tower: Jet/Lobe Transition, Wiggling, and the Magnetic Field Distribution. *ApJ*, 686:843–850, October 2008. doi: 10.1086/591222.
- J. S. Oishi and M.-M. Mac Low. The Inability of Ambipolar Diffusion to Set a Characteristic Mass Scale in Molecular Clouds. *ApJ*, 638:281–285, February 2006. doi: 10.1086/498818.
- P. Padoan, E. Zweibel, and Å. Nordlund. Ambipolar Drift Heating in Turbulent Molecular Clouds. *ApJ*, 540:332–341, September 2000. doi: 10.1086/309299.
- G. S. Patterson and Steven A. Orszag. Spectral calculations of isotropic turbulence: Efficient removal of aliasing interactions. *Phys. Fluids*, 14(11):2538–2541, 1971. doi: 10.1063/1.1693365.
- H. Politano and A. Pouquet. Model of intermittency in magnetohydrodynamic turbulence. *Phys. Rev. E*, 52:636–641, Jul 1995. doi: 10.1103/PhysRevE.52.636.
- H. Politano and A. Pouquet. Dynamical length scales for turbulent magnetized flows. *Geophys. Res. Lett.*, 25:273–276, 1998. doi: 10.1029/97GL03642.
- J. M. Scalo. Heating of dense interstellar clouds by magnetic ion slip - A constraint on cloud field strengths. *ApJ*, 213:705–711, May 1977. doi: 10.1086/155200.
- Zhen-Su She and Emmanuel Leveque. Universal scaling laws in fully developed turbulence. *Phys. Rev. Lett.*, 72:336–339, Jan 1994. doi: 10.1103/PhysRevLett.72.336.
- G. Tóth. Simulations of the Wardle Instability of C-Type Shock Waves. *Ap&SS*, 233:301–305, November 1995. doi: 10.1007/BF00627363.

- V. M. Uritsky, A. Pouquet, D. Rosenberg, P. D. Mininni, and E. F. Donovan. Structures in magnetohydrodynamic turbulence: Detection and scaling. *Phys. Rev. E*, 82:056326, Nov 2010. doi: 10.1103/PhysRevE.82.056326.
- E. G. Zweibel and K. Josafatsson. Hydromagnetic wave dissipation in molecular clouds. *ApJ*, 270: 511–518, July 1983. doi: 10.1086/161144.
- Ellen G. Zweibel. Ambipolar drift in a turbulent medium. *ApJ*, 567(2):962, 2002.
- Ellen G. Zweibel and Axel Brandenburg. Current sheet formation in the interstellar medium. *ApJ*, 478 (2):563, 1997.